R. van Hoften

The Mechanical and Chemical Characterization of a 3D Printed Inner Ear Implant

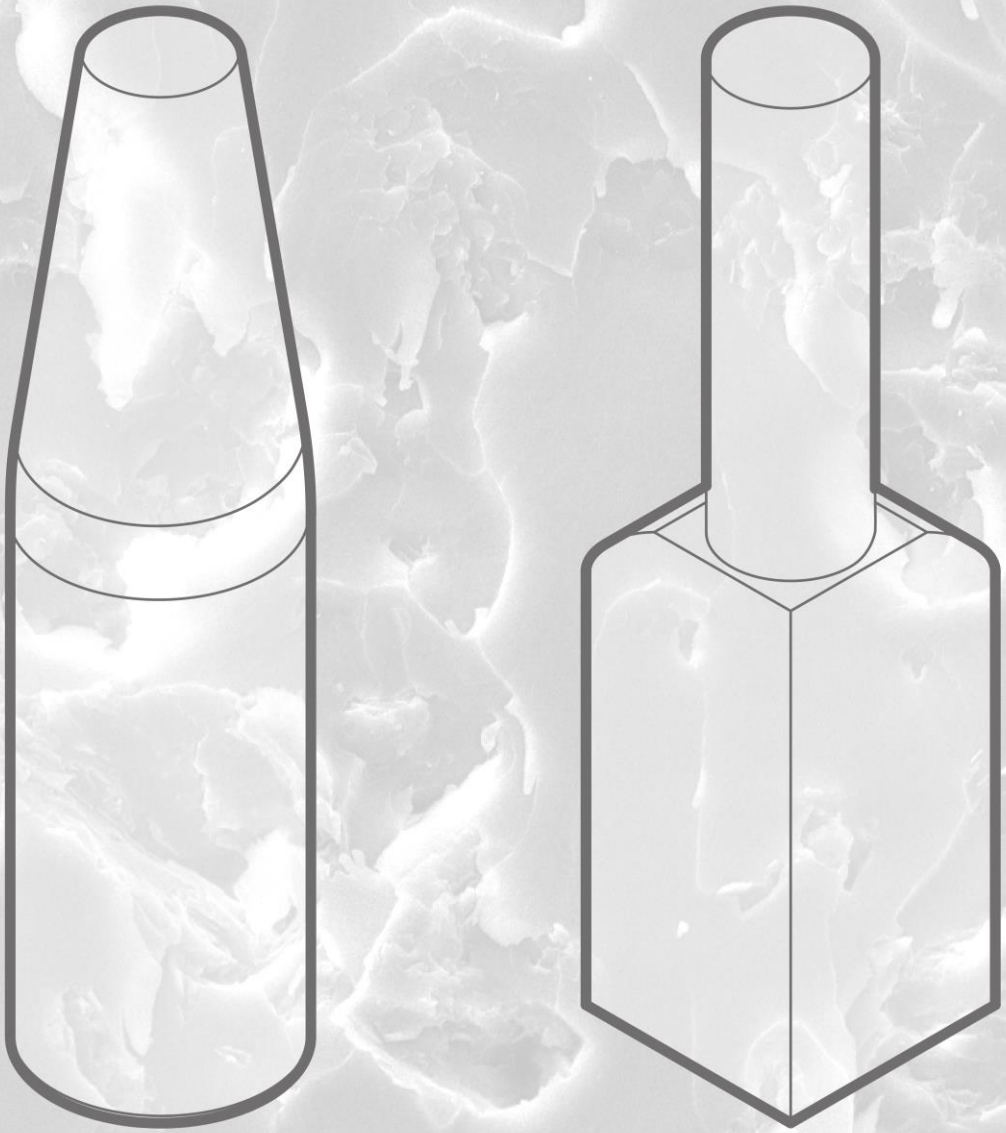

TU Delft

The Mechanical and Chemical Characterization of a 3D Printed Inner Ear Implant

By

R. van Hoften
4488415

in partial fulfilment of the requirements for the degree of

Master of Science
in Biomedical Engineering

at the Delft University of Technology,
to be defended publicly on Monday February 27th, 2023, at 9:15 AM.

Thesis committee:	Prof. dr. A. A. Zadpoor	TU Delft
	Dr. ir. E. L. Fratila-Apachitei	TU Delft
	Dr. ir. I. Apachitei	TU Delft
	Dr. M. J. Mirzaali	TU Delft
	Dr. ir. A. C. Akyildiz	TU Delft
	Dr. M. Ganjian,	TU Delft
	A. Isaakidou,	TU Delft

This thesis is confidential and cannot be made public until February 27th, 2025.

TU Delft

Contents

List of Abbreviations

2PP	Two-photon-polymerization
3D	3-dimensional
BLB	Blood-labyrinth-barrier
C3D8	Linear hexahedral element
C3D10	Quadratic tetrahedral element
C3D20R	Quadratic hexahedral element
CAD	Computer-aided design
C=C	Double carbon bond
C=O	Double carbon-oxygen bond
DC	Degree of conversion
DIC	Digital image correlation
DLW	Direct-laser-writing
EC	EarCube
FEA	Finite element analysis
GPa	Giga pascal
MPa	Mega pascal
OW	Oval window
RP	Reference point
RW	Round window
SD	Standard deviation
SEM	Scanning electron microscopy
SLA	Stereolithography
TM	Tympanic membrane
TPA	Two-photon absorption
TPMS	Triply period minimal surface
UV	Ultraviolet

Abstract

The current treatment for inner ear disorders most often involves systemic drug administration, which is associated with sub-therapeutic drug concentrations and side effects. A potential solution is an inner ear implant, which can provide targeted, local drug delivery for longer periods of time through implantation in the cochlea. Two implant designs, namely the EarCube and the BullEar, have been proposed for that purpose. They can be printed using two-photon polymerization with a novel photosensitive resin (IP-Q). Characterization of the mechanical behavior of material and the implant is needed to ensure its functionality and structural integrity. The material behavior of IP-Q was characterized by compression testing and resulted in a Young's modulus of 2.78 GPa. Furthermore, we used finite element analysis (FEA) modeling to simulate torsion testing on the implant. For experimental validation of the FEA model, scaled-up EarCubes were used. Three scaled-up EarCubes (with dimensions of $5 \times 5 \times 20$ mm^3, $10 \times 10 \times 40$ mm^3 and $20 \times 20 \times 80$ mm^3) were printed using stereolithography. For the linear part, the FEA model accurately simulated the experimental torsion testing of the scaled-up EarCubes. This experimental validation of the FEA model of the scaled-up EarCubes was extrapolated to the IP-Q, millimeter sized ($0.6 \times 0.6 \times 2.4$ mm^3) FEA model. For both implant designs, with two different inner porous structures, we characterized the linear part of the torsional behavior. When compared, the BullEar showed a higher stiffness and mechanical strength (roughly 3 times higher) than the EarCube. The difference in mechanical behavior for two different pore sizes in the inner structure was small. Therefore, we recommend the BullEar design (with either pore size) in further research.

Keywords: *Two-photon polymerization, FEA, stereolithography, inner ear implant, porous structure, torsion testing, compression testing, local drug delivery, IP-Q.*

Acknowledgements

I would like to start by thanking the Biomaterials and Tissue biomechanics group for the opportunity to do my master graduation project there. More specifically I would like to thank Dr. ir. E. L. Fratila-Apachitei for entrusting me with this project, and for the biweekly meetings full of feedback and advice. For these meetings, I would also like to thank Prof. dr. A. A. Zadpoor, Dr. ir. I. Apachitei and Dr. M. J. Mirzaali for taking the time to listen to my updates and providing feedback when needed. For my daily supervision, I would like to thank both Dr. M. Ganjian and A. Isaakidou, for the advice, support and the *gezelligheid* during all the long days in the lab. For all the help during the experimental testing, I would like to thank ir. M.A. Leeflang and ir. M. Cruz Saldivar. Last but not least, thanks to Iris for our daily routine of writing together, to Daan for the support with the design of some of the visuals and Tessel for the ever patient corrections of my English. To these people mentioned and the rest of my friends and family, thankyou for the moral support and love during this time.

1 Introduction

Symptoms such as sudden hearing loss, episodes of severe dizziness (*i.e.*, vertigo), or ringing in the ears (tinnitus) can all accompany inner ear disorders, such as Meniere's disease, which is one of the most common inner ear disorders. Meniere's disease is characterized by episodic, debilatating attacks, that can last from 20 min to 25 hrs [1-2]. Acorrding to estimates, Meniere's disease has been diagnosed in 190 out of every 100.000 people in the US as of 2010, usually in the age range of 40 to 55 years [1]. The first line of treatment for inner ear disorders is often systemic drug administration, due to its non-invasive nature. However, this approach is often associated with sub-therapeutic drug concentrations and side effects [3-4]. A solution to this issue could be local drug delivery, in which the drug is directly administered in or near the inner ear, but this presents its own unique challenges [4].

1.1 Anatomy and physiology of the ear

A basic understanding of the anatomy of the ear, the role of its separate parts, and the processes involved can help in identifying the challenges and opportunities in targeted drug delivery to the inner ear. The ear consists of three main parts, the external ear, the middle ear, and the inner ear (Fig. 1). The tympanic membrane (TM) separates the external ear from the middle ear and is (almost entirely) impenetrable [3]. The middle ear is an air-filled cavity, separated from the inner ear by the round window (RW) and the oval window (OW) and connected to the Eustachian tube, which is responsible for, ventilation, pressure equalization and clearance of secretions from the middle ear to the nasopharynx [5]. The inner ear consists of two main functional parts, the vestibular organ and the cochlear, responsible for balance and hearing respectively [3, 5]. The blood vessels supplying the inner ear are separated from the inner ear fluid spaces by the blood-labyrinth-barrier (BLB). This barrier helps maintain internal equilibrium in the ear and prevents pathogens from entering the inner ear. However, the protective function of this barrier also means that the drugs in circulation are prevented from entering the inner ear and only very limited amounts can enter the inner ear [3-4]. Therefore, an alternative method for drug delivery is required, such as local drug delivery to the inner ear.

Local drug delivery is the targeted delivery of drugs to a specific area of the body, to have an increased concentrations of drugs in the target area in comparison with the rest of the body.

This method is employed to maximize the efficacy of the drugs and minimize the side effects that occur due to systemic drug delivery.

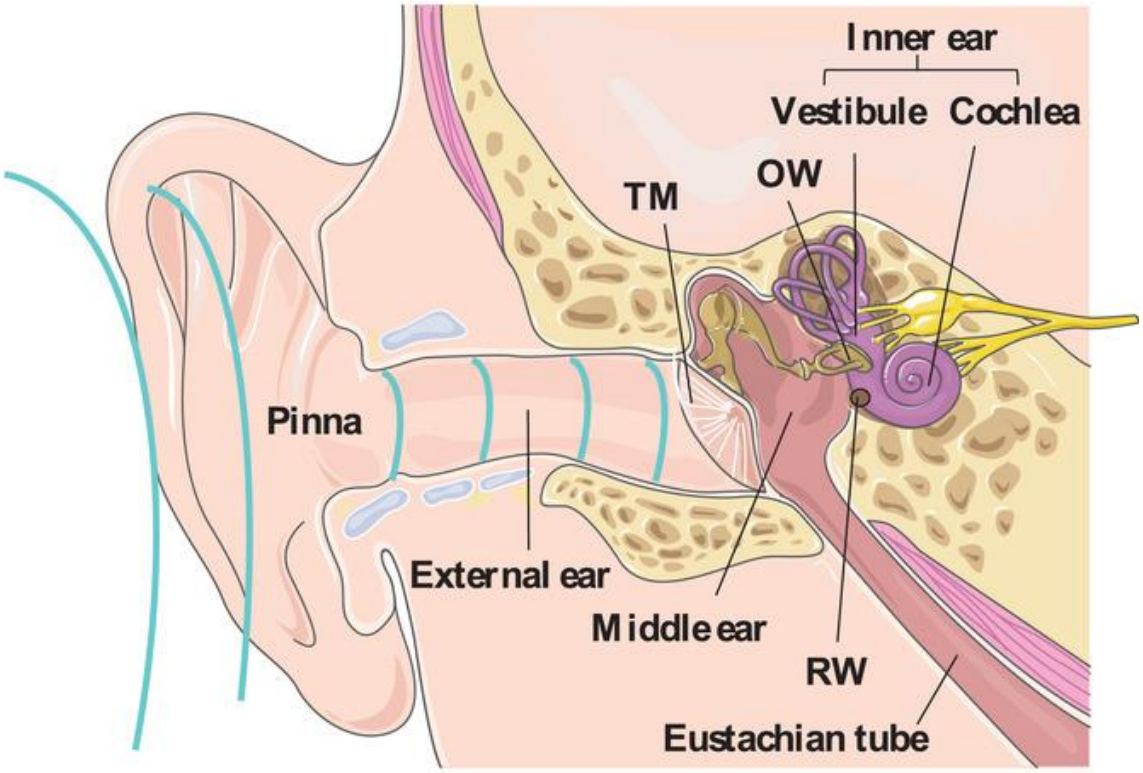

Figure 1. Schematic illustration of the anatomy of the human ear, consisting of the external, middle, and inner ear. The external and middle ear are divided by the tympanic membrane (TM). There are two openings from the middle ear to the inner ear, the round window (RW) and the oval window (OW). The Eustachian tube connects the middle ear to the back of the throat. The inner ear consists of two main functional parts, the vestibule and the cochlea [3].

1.2 Ear implant design for intracochlear drug delivery

Local drug delivery can be intratympanic (*i.e.*, drug delivery into the middle ear through the TM) or intracochlear (*i.e.*, a method which allows for direct drug entry into the cochlear) [5]. Intratympanic drug administration relies on the diffusion of the drug across the RW and the OW. This diffusion can be impacted by many different factors such as the permeability of the windows membranes. Effective drug delivery with intratympanic administration is limited by short retention time of the drugs, due to clearance by the Eustachian tube [4-5]. Intracochlear administration, which bypasses the permeability of the RW and OW, is more efficient, as it allows for direct drug entry into the cochlear. Intracochlear administration can be achieved by injections, however care must be taken not to damage the cochlea during the procedure.

Another option for intracochlear administration, which avoids repeated injections, is a drug delivery device which can be implanted in the cochlear [5]. One of the requirements for such a drug delivery device is that it can remain in the cochlear for longer periods of time, to avoid repeated trauma to the cochlea. Therefore, it should have an internal drug reservoir, which can

provide reliable residence times of the drugs in the inner ear [4, 6]. The drug delivery device can be inserted into the OW or RW. To this end, two potential designs have been proposed for this ear implant, the first of which is referred to as the EarCube (Fig. 2A). The EarCube design consists of a cylindrical part, which goes into the OW or RW, and a cubic part, which serves as a drug reservoir and remains in the middle ear. To allow for drug storage and diffusion of the drug, the EarCube design is porous on the inside. This inner porous structure should allow for sufficient drug storage and diffusion while the implant remains mechanically stable.

There are two different porous designs proposed for the EarCube, which are thought to determine and influence the amount of drug storage, the diffusion of the drugs, and the mechanical properties of the EarCube. For both EarCube designs, the inner structure consists of an interconnected network of square unit lattices, which has pores and support beams of equal width. The first inner porous structure has pores with sizes of $20 \times 20 \times 20\ \mu m^3$ (Fig. 2B), and the other structure has pores with sizes of $60 \times 60 \times 60\ \mu m^3$ (Fig. 2C). These inner structures are the same in the second proposed design for the ear implant, which is referred to as the BullEar (Fig. 2D, 2E, 2F). The BullEar's different geometry is expected to enhance its mechanical properties. The EarCube has an abrupt change in cross-section size at the juncture between the cylindrical and cubic part. This abrupt change in cross-section can lead to stress concentrations at this part of the design. In the BullEar design, this abrupt change in cross-section is not present, as the diameter of the design gradually decreases, which should reduce stress concentrations.

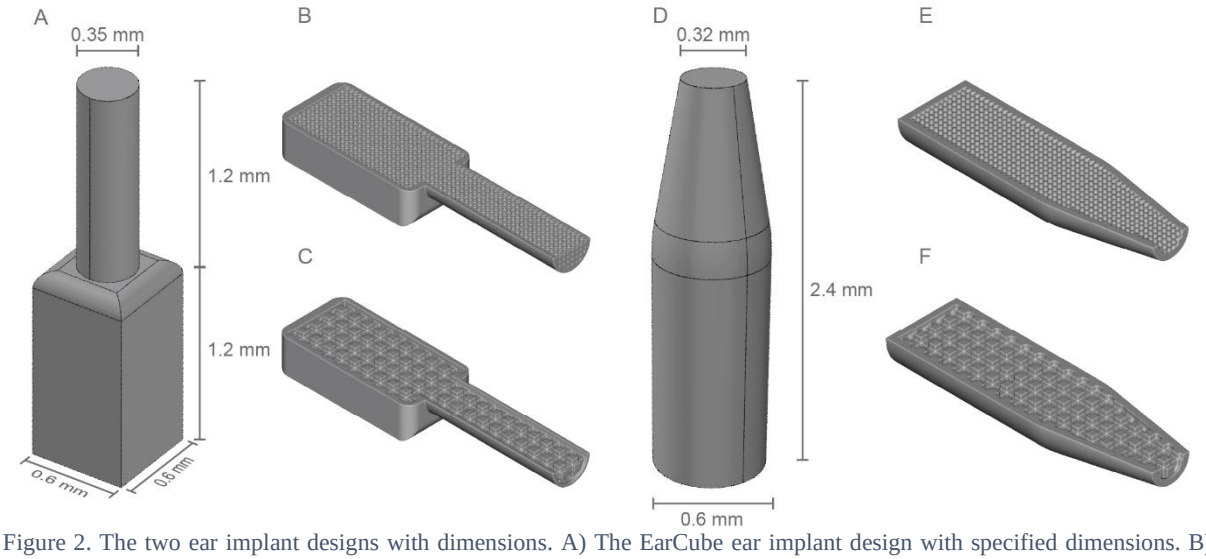

Figure 2. The two ear implant designs with dimensions. A) The EarCube ear implant design with specified dimensions. B) Internal view of the EarCube with the inner porous cubic lattice structure with $20 \times 20 \times 20\ \mu m^3$ pores. C) Internal view of the EarCube with the inner porous cubic lattice structure with $60 \times 60 \times 60\ \mu m^3$ pores. D) The BullEar design with specified dimensions. E) The internal view of the BullEar inner porous cubic lattice structure with pores of $20 \times 20 \times 20\ \mu m^3$. F) The internal view of the BullEar inner porous cubic lattice structure with pores of $60 \times 60 \times 60\ \mu m^3$.

1.3 Manufacturing of the ear implant

Due to the size of the ear implant, (*i.e.*, 600 × 600 × 2400 μm^3) its fabrication is not straightforward using traditional manufacturing methods [7]. A solution to this problem could be the use of additive manufacturing. While for most additive manufacturing techniques the size difference between the inner porous structure and the overall size (a factor of 120 for the smallest pore size) would be challenging, this could be realized using the direct-laser-writing (DLW) technique based on two-photon polymerization (2PP) [8]. 2PP is based on the phenomenon of two-photon absorption (TPA); a process where two photons are simultaneously absorbed and a molecule is excited to a higher state [9]. TPA only occurs in the presence of high-intensity light source (such as a laser) and is quadratically dependent on the local light intensity:

$$\frac{dI(z)}{dz} = -\beta I^2(z) \qquad 1.1$$

where I is the light intensity, z is the propagation direction and β the TPA coefficient. This quadratic dependency combined with the small cross-section of TPA, allows for spatial confinement of the excitation [10]. When TPA occurs in a photosensitive resin, the excitation of the molecule initiates the polymerization reaction in the resin. The polymerization occurs only if the threshold of the photoresin is reached, which, for TPA, only occurs in or near the focal spot, in a small volume referred to as the voxel, which allows for high resolution printing (Fig. 3). By moving the laser focal spot through the photosensitive resin (according to a predetermined 3D computer-aided design (CAD)) it becomes possible to create high-resolution (below the diffraction limit) 3D structures [9-10].

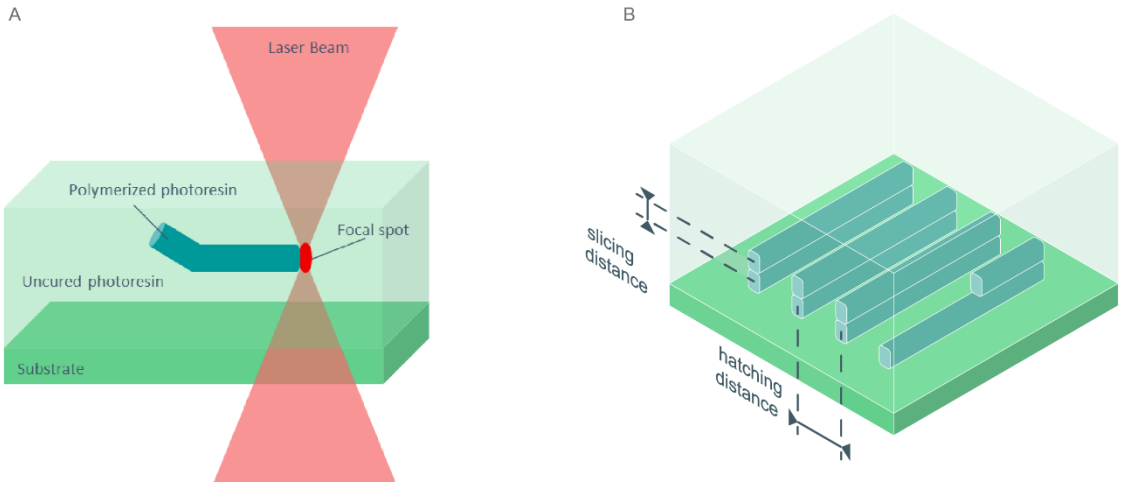

Figure 3. (A) Schematic of 2PP process showing the focal spot where the threshold is reached for polymerization of the photoresin, which is located on top of the substrate. (B) A schematic representation of the hatching and slicing distance, printing parameters which can be varied during the 2PP process.

There are a variety of photosensitive resins which can be used for 2PP. In the context of the current research, the material of interest is a methacrylate-based polymer called IP-Q (Nanoscribe GmbH, Germany). It is a commercial photosensitive, negative-tone resin specifically designed for the high-speed fabrication of millimeter-sized objects [11]. IP-Q is a relatively new resin, and as a result, little is known about its material properties. Schweiger *et al.* published the first paper on IP-Q, investigating the Young's modulus of IP-Q in correlation to the printing process parameters used [12]. These parameters affect the polymerization of the resin, and consequently the mechanical properties of the printed material [13-17].

1.4 Chemical characterization of photoresins

The polymerization that occurs during 2PP has the same basic principles for all photoresins, although the precise reaction kinetics may vary depending on the specific material [13-14]. A photoresin typically consists of a (meth)acrylic monomer and a photo-initiator. The photo-initiator in the resin absorbs the energy of the two incoming photons, initiating the polymerization reaction. This causes the double carbon bond (C=C) to break and forms the (meth)acrylic polymer (Fig. 4).

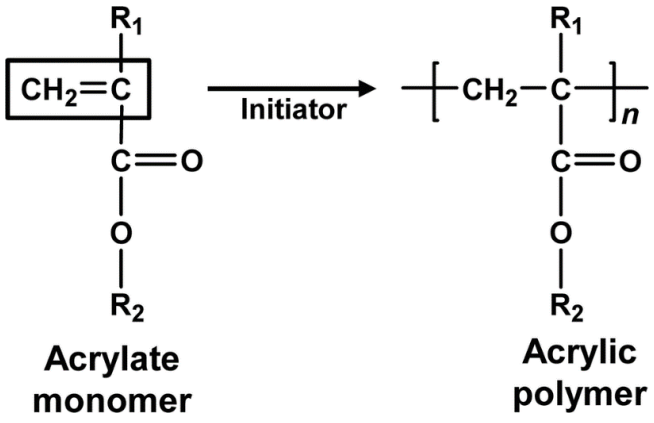

Figure 4. The synthesis of an acrylic polymer. Acrylic monomers containing a carbon double bond become acrylic polymers trough free-radical polymerization [18].

The extent of the polymerization can be determined by comparing the amount of C=C in a photoresin before and after polymerization. As the C=C bond breaks and converts to a single carbon bond (C-C) during polymerization, the double carbon oxygen bond (C=O) remains unchanged upon polymerization and can be used as an internal reference (Fig. 4). The degree of conversion (DC), which is related to the crosslinking of the polymers [19], is used to quantify the amount of C=C consumed during polymerization. This is calculated by comparing the change in C=C bond to the change in C=O bond between a polymerized and unpolymerized sample [15,19-20]. The DC can be determined using Raman spectroscopy, a method that

measures the vibrational modes of molecules and identifies distinctive peaks for different intramolecular bonds. The C=C vibrational mode has a peak at roughly 1640 cm^{-1}, while the C=O vibrational mode shows a peak at 1715 cm^{-1} [19-20]. However, for different photoresins there might be slight shifts between the peaks, or Raman spectra might have additional peaks, such as the peak at 1590 cm^{-1} for the aromatic ring [21]. As the DC is the measure of polymerization in the photoresin, it is also related to the mechanical properties of the printed material [13–15, 19].

1.5 Mechanical characterization

Before implantation of the ear implant is feasible, the mechanical properties of the material and of the implant need to be characterized. This is done to verify that the implant is strong enough to withstand the mechanical stresses that may occur during and after implantation. According to an expert surgeon in this medical field, the likely method of implantation will involve twisting the ear implant into a hole created in the cochlea. This twisting means that the ear implant will be subjected to torque, therefore the torsional behavior of the implant must also to be characterized.

The mechanical properties of a material can be determined through mechanical testing methods, such as tensile or compression testing. However, most standard testing machines require larger volumes of specimens to be able to perform these tests, which can be difficult to obtain using 2PP [17]. Compression testing and nanoindentation can be performed on small 2PP printed structures using nanoindenters [14-15, 21]. So far, IP-Q has only been experimentally tested using nanoindentation [12]. More complex mechanical testing such as torsion testing cannot currently be performed on the ear implant due to its small size (600 µm Ø × 2400 µm). Scaling up the ear implant could help overcome this issue. However, this is not possible using 2PP. Other additive manufacturing techniques, such as stereolithography (SLA), can print larger, scaled-up ear implants, which would be able to undergo torsion testing. SLA is similar to 2PP, in that it also uses a light-sensitive resin that is exposed to light, which triggers the polymerization reaction, that forms chains of polymers and consequently solidifies the resin [22].

Another way to determine the mechanical behavior of an ear implant is by using Finite Element Analysis (FEA), which is not limited by size. FEA is a numerical method which can be used to predict mechanical behavior such as the torsional behavior of the ear implant. The previously

mentioned scaled-up ear implants can be used to provide experimental validation of the FEA simulation. If the FEA simulation models the experimentally tested solid, scaled-up, SLA printed ear implants closely, it is more reasonable to assume the simulation of torsion testing of the 600 µm Ø × 2400 µm IP-Q ear implants is predicting their real behavior. For FEA simulations to be accurate, input data such as the Young's modulus and the stress-strain curve of the material to be simulated is needed. This can be provided by performing mechanical testing, such as compression or tensile testing, for both SLA and 2PP resins.

The goal of this thesis is to explore the effect of polymerization on the chemical structure of IP-Q and to characterize the mechanical behavior of the IP-Q ear implant. For clarity and ease of reading this thesis has been divided into five main sections, of which this introduction is section 1. In section 2, the experimental and numerical methods used are explained, as well as the specimen designs, manufacturing, and materials. In section 3, the results are presented. Firstly, the chemical characterization of IP-Q using Raman spectroscopy is explored, after which the mechanical characterization of the ear implant is presented. The experimental torsion testing results of the scaled-up ear implants made with grey resin are compared to the FEA simulation results and FEA simulations for solid and porous designs for both the EarCube and the BullEar are presented. In section 4, these results are discussed and recommendations for future work are given and finally, in section 5, the conclusions are summarized.

2 Materials and Methods

2.1 Specimens for Raman spectroscopy

The commercial photopolymer IP-Q (Nanoscribe GmbH, Germany) was chemically analyzed using Raman spectroscopy, to determine the chemical properties of IP-Q before and after the two-photon polymerization process. For this reason, two types of specimens were used for Raman spectroscopy, polymerized and unpolymerized IP-Q resin. The polymerized IP-Q resin was a pillar with a diameter of 5 µm and height of 200 nm and was fabricated on a silicon substrate using the Photonic Professional TG machine (Nanoscribe GmbH, Germany). The laser power was set to 100% (50 mW), the writing speed was 100.000 µm/s, the slicing distance was 4.98 µm and the hatching distance was 1 µm. For unpolymerized IP-Q resin, a few drops of the resin were applied to the surface of a 1 × 1 cm^2 silicone substrate just before analysis.

2.2 Chemical analysis of IP-Q using Raman spectroscopy

The two samples (polymerized and unpolymerized IP-Q) were analyzed using the inVia Reflex Raman system (Renishaw, UK), with a 50 × objective and an excitation wavelength of 532 nm. For both specimens, Raman spectra were acquired with a laser intensity of 50%, an exposure time of 1.0 sec averaged over 15 acquisitions. After the acquisition of the spectra, baseline correction was performed. For each specimen, three separate measurements were performed, which were subsequently averaged.

2.3 Specimens for compression testing

For compression testing pillars with an aspect ratio of 2 (*i.e.*, the height is two times larger than the diameter,) were printed. The pillars were printed using two different additive manufacturing techniques (*i.e.*, SLA and 2PP) with the different materials, namely grey resin, and IP-Q.

2.3.1 SLA printed pillars

SLA and 2PP are based on the similar mechanisms of photopolymerization, where a light-sensitive resin, is exposed to UV or visible light. This light triggers the polymerization reaction, which creates chains of polymers and forms a solid resin. In SLA printing a platform is immersed in a transparent tank filled with a light-sensitive resin. The laser beam traces the design on the area and, after each layer is formed the platform moves upward by a constant amount, which is the height of the layer, known as the layer thickness [22]. The precision of SLA printing is related to the laser spot size; in the case of the Form 3+, the XY resolution is 25 μm and the laser spot size is 85 μm. The pillars were printed with a diameter of 8 mm and a height of 16 mm, using grey resin (Formlabs, USA) on the commercial system Form3+ (Formlabs, USA) via SLA. This material and technique were chosen due to the expected similarity of material properties to IP-Q and the similarity of the manufacturing process of SLA to the process of 2PP. The pillars were printed with two different layer thicknesses of 25 and 50 μm, for two different print orientations. One print orientation had horizontal layers, while the other orientation was composed of lateral layers, which is a 90 degrees difference in orientation (Fig. 5). Three specimens were printed for each condition After printing the pillars were rinsed in IPA for 10 min, then post-cured at 80 °C for 15 min, according to the recommended rinse and cure times by Formlabs. The dimension (height and diameter) of the pillars after printing were measured using a caliper with a precision of 0.05 mm.

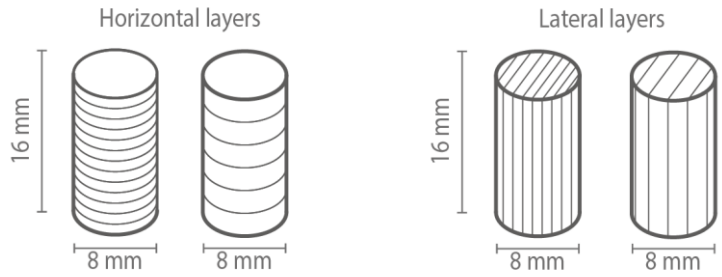

Figure 5. Schematic of the SLA pillars, printed with horizontal layers (left) and lateral layers (right) for a layer thickness of 25 µm and 50 µm.

2.3.2 2PP printed pillars

The IP-Q pillar was printed by a colleague of the Biomaterials and Tissue biomechanics group. The printed pillars, with a height of 100 µm and a diameter of 50 µm, were printed using the Photonic Professional TG machine (Nanoscribe GmbH, Germany). The laser power set to 100% (50 mW), a writing speed of 100.000 µm/s, a hatching distance of 1 µm and a slicing distance of 4.98 µm. These are the same settings as for the specimens printed for chemical analysis.

2.4 Mechanical characterization of the materials grey resin and IP-Q

2.4.1 Compression testing for SLA specimens

The pillars were compressed using the Electropulse™ E10000 (Instron Systems, USA) with a speed of testing of 1.3 mm/min (according to the ASTM D695-15 [23]), until a maximum force of 8500 N was reached. To improve the accuracy of the measured displacement by compression, a DIC (digital image correlation) system was used (Q-400 2 × 12 MPixel, LIMESS GmbH, Germany) at a frequency of 1 Hz (Fig. 6). Prior to testing, the specimens were first painted whit and then a black dot speckle pattern was applied to track the displacement of the specimen. The stress and strain of each specimen was calculated using a commercial program (Instra 4D v4.6, Danted Dynamics A/S, Denmark). The Young's modulus was calculated from the elastic region of the engineering stress and strain region, between a strain of 0.3 and 2% and the result was averaged for the three specimens. The yield strength (σ_y) was calculated as a 0.2% offset yield. The true strain was calculated from the engineering strain using the following equation [24]:

$$\varepsilon = ln\left(1 + \varepsilon_{eng}\right) \tag{2.1}$$

where ε is the true strain and ε_{eng} is the engineering strain. The true stress was calculated from the engineering stress according to eq. 2.2 [24]:

$$\sigma = \sigma_{eng}\left(1 + \varepsilon_{eng}\right) \tag{2.2}$$

where σ is the true stress and σ_{eng} is the engineering stress. To define plasticity in Abaqus for FEA the true plastic strain of a material is required as input and is defined as follows [24]:

$$\varepsilon^{pl} = \varepsilon^{t} - \varepsilon^{el} = \varepsilon^{t} - \frac{\sigma}{E} \tag{2.3}$$

where ε^{pl} is the plastic true strain, ε^{t} is the true total strain, ε^{el} is the true elastic strain and E is the Young's modulus.

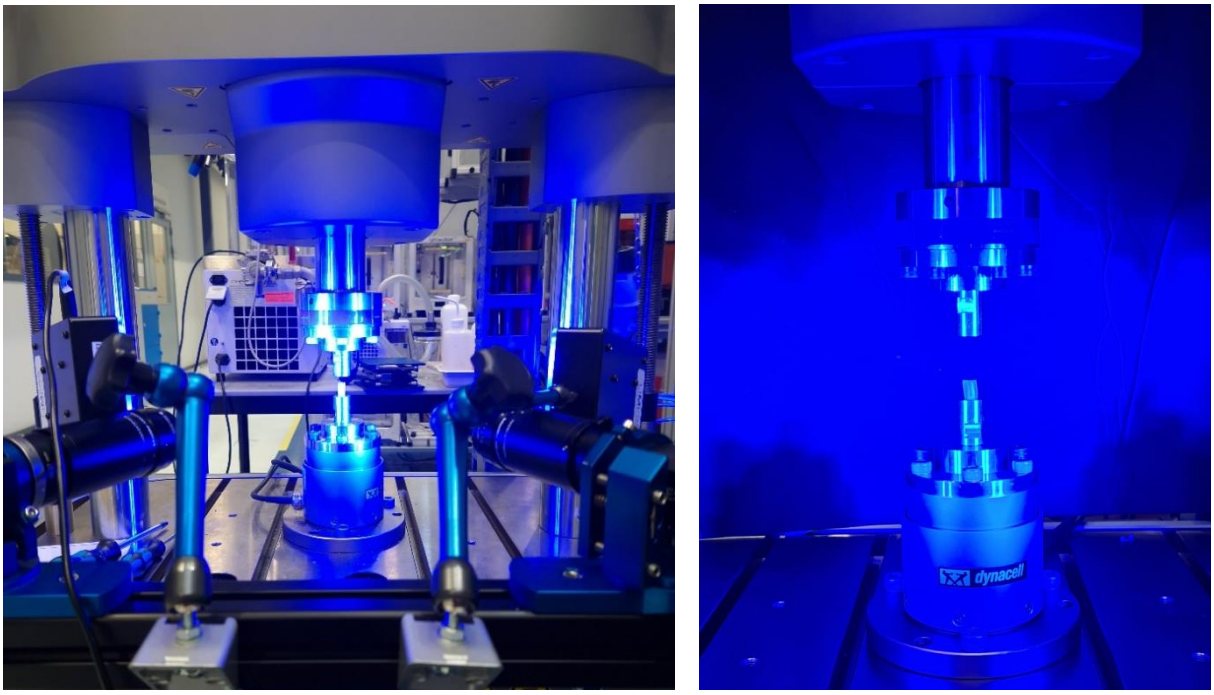

Figure 6. Images of the setup for compression testing of SLA printed pillars with the Electropulse E10000 and the DIC system.

2.4.2 Compression of IP-Q pillars

The compression testing on the IP-Q pillars was performed in Switzerland, by the EMPA research institute. The true stress and true plastic strain were calculated in the same way as for the grey resin SLA printed pillars.

2.5 Design of the ear implants

2.5.1 Solid ear implants

There are currently two different designs for the ear implant, namely the EarCube and the BullEar (Fig. 7).

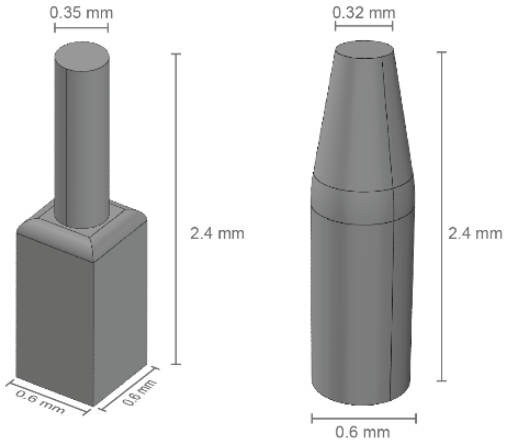

Figure 7. The two different designs for the ear implants, the EarCube (left) and the BullEar (right).

2.5.2 Porous ear implants

The final ear implant will have a hollow structure inside, to allow for drug storage and release. The inner structure consists of an interconnected network of square unit lattices, with pores with a size of 20 × 20 × 20 μm^3 or 60 × 60 × 60 μm^3 (Fig. 8).

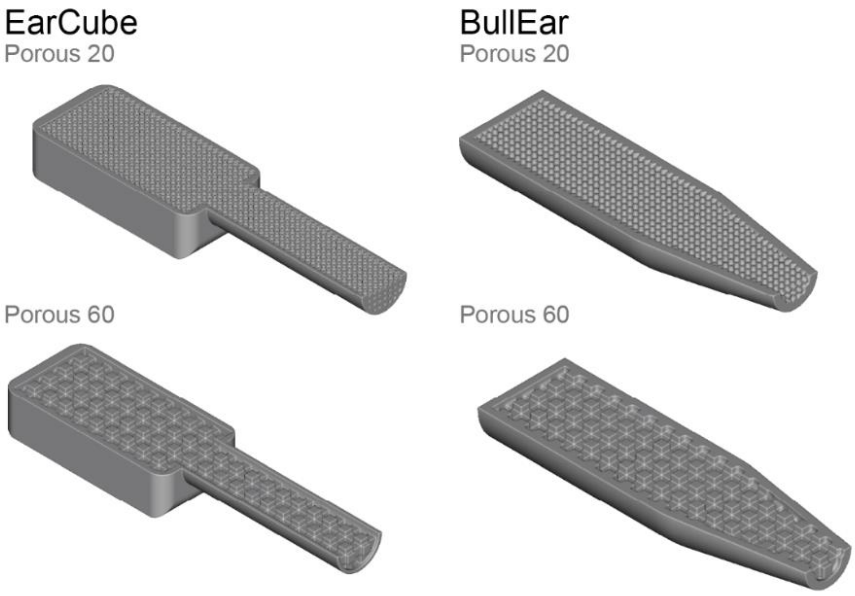

Figure 8. The two different pore sizes for both the porous implants (EarCube on the left, BullEar on the right) of respectively 20 and 60 µm.

2.6 Specimens for torsion testing

The designed Ear implant has the dimensions of 2.4 × 0.6 × 0.6 mm^3 (l × w × h). However, the mechanical characterization of an implant at this scale is not straightforward. For instance, universal testing machines cannot be used unless the ear implants are fabricated at a larger scale. 2PP printing can only produce prints up to a few mm, therefore it cannot be used for printing

larger ear implants. An alternative approach is to use FEA to investigate the mechanical behavior of the ear implants. Using FEA, the implants can be modeled for any size or material. However, experimental testing is needed for the validation of the FEA model. SLA, which has a maximum print size of 145 × 145 × 185 mm^3 [25], can be used to validate the FEA models of the larger, upscaled specimens and be extrapolated to the FEA model of the ear implant with the dimensions of 2.4 × 0.6 × 0.6 mm^3.

2.6.1 Torsion specimen design for SLA

For the experimental torsion testing, only the EarCube was scaled up. The scaled up EarCube was designed in three different sizes (Table 1, Fig. 9), referred to as EC8, EC16 and EC32. The EC refers to EarCube and the number is roughly the factor by which the EarCubes are scaled up. The scale factor difference for the scaled-up EC's is two. All the three sizes were designed as fully solid structures and, additionally, the EC32 torsion specimen was also printed with an inner porous structure. The inner porous structure was the same as the porous 60 structure, except now 32 times larger, giving the pore size of 1.9 × 1.9 × 1.9 mm^3.

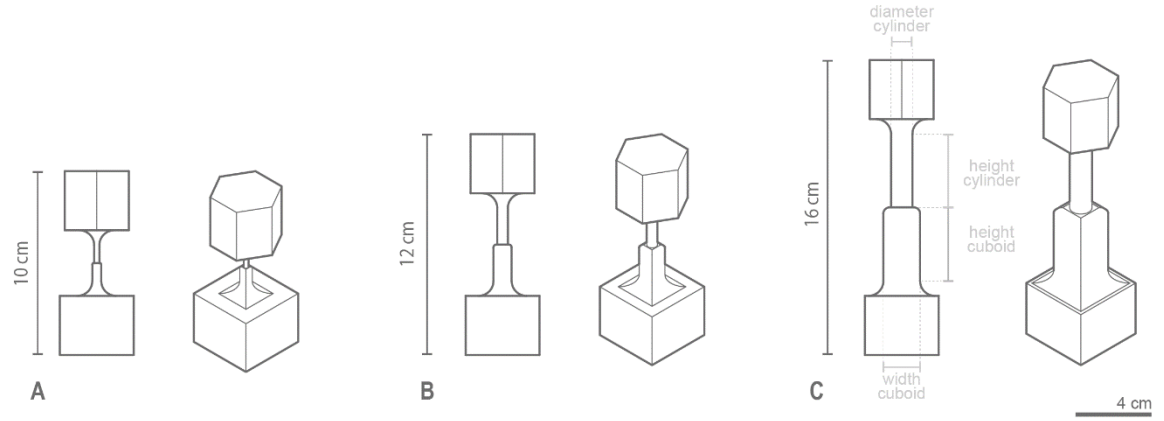

Figure 9. The torsion specimen designs for the EarCube with additional grippers to make torsion testing possible in EC32, with total length × width of 16 × 4 cm^2 (A), EC16 with a total length × width of 12 × 4 cm^2 (B) and EC8 with a total length × width of 10 × 4 cm^2 (C).

Table 1. The print design dimensions of upscaled EarCube implants. A visual representation of these dimensions can be found in Fig. 9.

Specimen	*Width × length cuboid (mm^2)*	*Height cuboid (mm)*	*Diameter cylinder (mm)*	*Height cylinder (mm)*
EC8	4.85 × 4.85	9.7	2.83	9.7
EC16	9.85 × 9.85	19.7	5.75	19.7
EC32	19.85 × 19.85	39.7	11.58	39.7
Porous EC32	19.85 × 19.85	39.7	11.58	39.7

Additional grippers to the bottom and top part of the EarCube were added to be able to perform torsion testing (Fig. 9) and were designed to fit exactly into steel holders (Fig. 10) compatible with the Instron E10000. These additional grippers are the same size for all three scales of the upscaled EarCube. The bottom part, which attached to the cubic part of the EarCube, is a square prism with dimensions of 39.85 × 39.85 × 31.88 mm^3. To the top part of the EarCube, the cylindrical part, a hexagonal prism with sides of 19.93 mm and a height of 31.88 mm was added. To make the transition from the EarCube to the grippers less sharp, additional fillets were designed and added to avoid stress concentration in the junctures. The total structure of EarCube plus grippers will be referred to as the torsion specimens from here on out.

Figure 10. Image of the steel holders. On the left the top part of the steel holders with the hexagonal prism and on the right the bottom part with the square prism.

2.6.2 Torsion specimen printing

The torsion specimens were fabricated using SLA, on a Form 3+ commercial system, the same as was used for the compression specimens. Preform, the 3D printing software from Formlabs, was used to autogenerate support structures to pass the printability check. The specimens (both solid and porous) were printed with a layer thickness of 50 μm, using the photopolymer grey resin, which was also used for compression testing. After printing, the support structures were removed, and the specimens were rinsed in IPA for 10 min and then post-cured at 80 °C for 15 min according to the recommended rinse and cure times by Formlabs. The porous EC32 specimens required some small additional support structures inside the porous structure and were not able to be removed.

2.6.3 Specimen dimensions post printing

The printed torsion specimen dimensions were measured using a caliper with a precision of 0.05 mm (Table 2). The total height is the height measured between the hexagonal and square prism and includes the height of the EarCube and the fillets.

Table 2.The measured dimensions of the torsion specimens printed with grey resin.

Specimen	*Width cuboid (mm)*	*Cylinder Ø (mm)*	*Total height (mm)*
EC8_2	5.0	3.0	35.55
EC8_3	5.0	2.95	35.15
EC8_4	5.0	3.0	35.25
EC8_5	5.0	2.95	35.4
EC16_1	10.0	5.85	55.0
EC16_3	10.05	5.9	54.85
EC16_4	9.95	5.9	55.1
EC32_1	20.0	11.7	95
EC32_2	20.0	11.75	94.8
EC32_3	20.05	11.75	94.9
EC32_4	20.1	11.75	94.9
Porous EC32_1	20.35	11.45	84.8
Porous EC32_2	19.85	11.4	85.3
Porous EC32_3	19.9	11.45	85.2

2.7 Experimental mechanical characterization of the EarCube

2.7.1 Torsion testing

Torsion testing was performed using the Electropulse E10000 fitted with the steel holders, in which the specimens were placed. The torsion specimens were rotated with a shear strain rate of 0.001 s^{-1} for each of the specimens, to have a high enough speed of testing to make creep negligible according to ASTM E143-20 [26]. To obtain the same strain rate for the three different sized solid specimens and the porous specimen, the rotation speed differed accordingly and were calculated with eq. 2.4:

$$\gamma = \frac{\theta r}{L} \tag{2.4}$$

where γ is the shear strain, θ is the rotation, r is the radius and L is the total printed height of the specimens. The rotation speed needed for a constant strain rate for the three sizes of the torsion specimens was converted to rad / s (Table 3). The torque (Nm) and rotation (deg) were recorded until the failure of the specimen or until one of the two limits set was reached. The limit for rotation was 270° and the limit for the torque was 95 Nm. To improve the accuracy of

the measured displacement by rotation, the same DIC system as for compression was used again to calculate the shear strain.

Table 3. The rotation speed and strain rate for the three sizes of solid torsion specimens and the porous specimen.

Specimen	*Rotation speed (rad/s)*	*Shear strain rate (s^{-1})*
EC8	0.0238	0.001
EC16	0.0183	0.001
EC32	0.0158	0.001
Porous EC32	0.0149	0.001

2.7.2 Investigating the failure mode of the solid torsion specimens

Images were taken from the bottom part of the torsion specimens after torsion testing, from these images the angles of the specimens were determined when possible. For two specimens, namely EC8_2 and EC8_4, SEM images of the surface of the fracture angles were taken.

2.7.3. Calculating shear stress and strain

The shear stress was calculated from the measured torque using eq. 2.5:

$$\tau = \frac{Tr}{J} \tag{2.5}$$

where τ is the shear stress and J is the second polar moment of area. The polar moment of area for the EarCube was calculated for smallest cross-sectional area, the cylindrical part of the EarCube. This is because the assumption is that the stress will mainly occur in the part of the implant with the smallest cross-sectional area. The second polar moment of area was calculated using eq. 2.6:

$$J = \frac{\pi D^4}{32} \tag{2.6}$$

where D is the diameter of the cylinder. The measured values of the diameter of the cylinders of the torsion specimens were taken from (Table 2). The strain was calculated using the displacement values obtained using the DIC system. The displacement of two points on the cylinder (near the base and near the top) were measured (Fig. 11). This displacement was converted into rotational displacement θ (rad). The difference in rotation between the two points was calculated by subtracting the rotation from the bottom point from the top point. The shear strain was then calculated with eq. 2.4 using this rotational displacement.

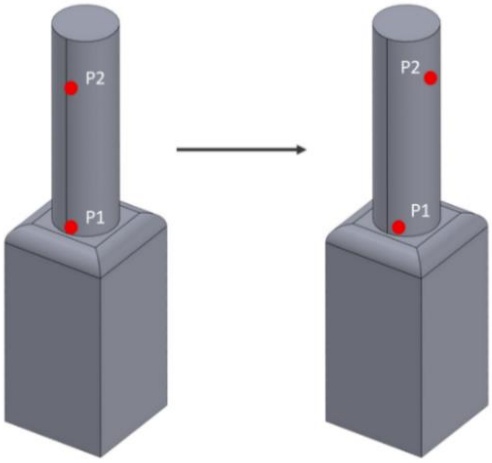

Figure 11. Representation of the displacement recorded from two points with DIC. The rotation of P2 and P1 was calculated separately and the rotation of the section of the cylinder was taken as the difference of the rotation between the two points.

2.8 FEA mechanical characterization of the ear implant

The mechanical behavior of an ear implant can be modeled using FEA. However, to do so accurately, the mechanical characteristics of the material, such as the Young's modulus and the stress-strain curve, must be known. Torsion testing was modeled on the upscaled EarCubes (without the additional grippers), on the torsion specimens and on the EarCube and the BullEar with dimensions 0.6 × 0.6 × 2.4 mm^3. For the real sized ear implants, torsion testing was modeled on both solid and porous implants (for both the EarCube and the BullEar) with pore sizes of 20 and 60 μm. The FEA simulations were performed using the commercial software Abaqus/CAE (Dassault Systèmes SE, France).

2.8.1 Torsion on a Cylinder

To start, the torsion testing was modeled on a simple cylinder with a diameter of 10 mm and a height of 20 mm. The output of the FEA simulation was the torque (in this case the reaction moment) needed to rotate the cylinder and the shear stress of the cylinder after rotation. The material properties of grey resin were assigned as E = 2504 MPa (obtained from the compression testing of grey resin pillars) and ν =0.45 (Poisson's ratio). Thereafter, two reference points (RP) were generated, located at the center of the top and bottom part of the cylinder, named RP-1 and RP-2, respectively. The surface of the top and bottom part was then coupled to the reference point using kinematic coupling (Fig. 12), which constrains the motion of the coupled nodes to the rigid body motion of the reference point.

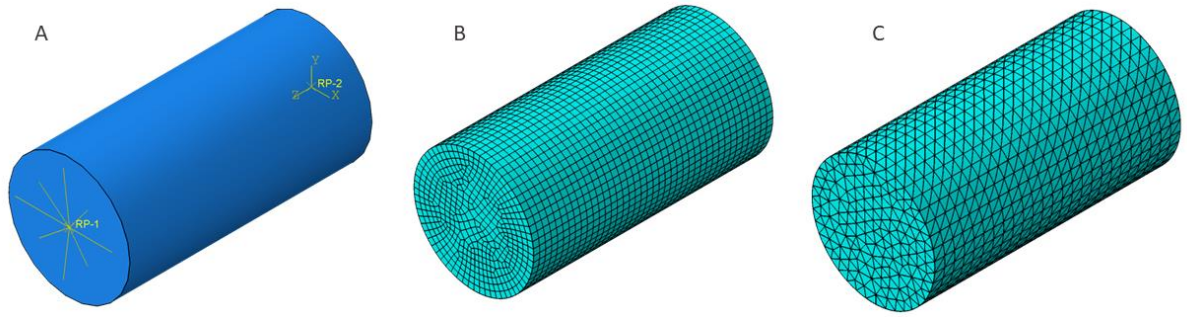

Figure 12. Cylinder modeled in Abaqus with (A) the two reference points (RP-1 and RP-2) on the top and bottom, respectively. (B) The cylinder with the hexahedral elements (C3D8 and C3D20R). (C) The cylinder with the tetrahedral elements (C3D10).

Thereafter, two boundary conditions were created to simulate torsion. RP-2, located at the bottom of the cylinder, was encastered, meaning that no translation (U) or rotation (UR) in any direction was allowed (U1 = U2 = U3 = UR1 = UR2 = UR3 = 0). RP-1, located at the top of the cylinder, was rotated by 0.2 radians. The cylinder is modeled in the linear region, so the material obeys Hooke's law, and the angle of twist equation holds true:

$$\theta = \frac{TL}{GJ} \tag{2.7}$$

where θ is the angle of twist and G is the shear modulus. To determine the size of the mesh required for accurate results, a mesh convergence study was performed on the cylinder using quadratic tetrahedral elements (C3D10) and two types of hexahedral elements (C3D8 and C3D20R), which were linear and quadratic, respectively. The convergence study evaluated both the reaction moment (RM3) and the shear stress (S23). The theoretical value of the torque (reaction moment in this case) for a rotation of 0.2 rad was calculated using eq. (2.7). The shear modulus can be calculated using eq. 2.8:

$$E = 2G(1 + \nu) \tag{2.8}$$

where ν is the Poisson's ratio.

2.8.2 Torsion on solid ear implants

The solid ear implant models and torsion specimen models were created in SolidWorks (Dassault Systèmes SolidWorks crop., Waltham, MA, USA) and subsequently imported as .STEP files in Abaqus/CAE. Torsion testing was performed in the same way as for the cylinder, but with the nonlinear geometry turned on and a plasticity component for the material property was added. The Young's modulus, the Poisson's ratio, the true stress, and true plastic strain curve were added to all models. The true stress and true plastic strain were calculated using equations 2.2 and 2.3, respectively, from the experimental compression data of grey resin and

IP-Q. From the FEA models the torque and the rotation were extracted at RP-2. The shear stress and strain were extracted from the top of the cylinder or the BullEar farthest away from the center, as this is where the shear stress and strain are largest according to eq. 2.4 and 2.5.

2.8.3 Torsion on porous ear implants

The porous models were created by converting the .stl files, using a Matlab and python script according to the methodology described by Saldivar et. al., into a hexahedral element mesh in Abaqus [27]. The torsion testing was performed in the same way as for the solid FEA models and the same material property values for IP-Q and grey resin were used. The torque, rotation, shear stress and shear strain were extracted in the same way as for the solid models.

3 Results

3.1 Comparison of polymerized and unpolymerized IP-Q via Raman spectroscopy

The difference between the Raman spectra of an unpolymerized IP-Q sample and a polymerized sample shows the effect the polymerization process has on IP-Q (Fig. 13).

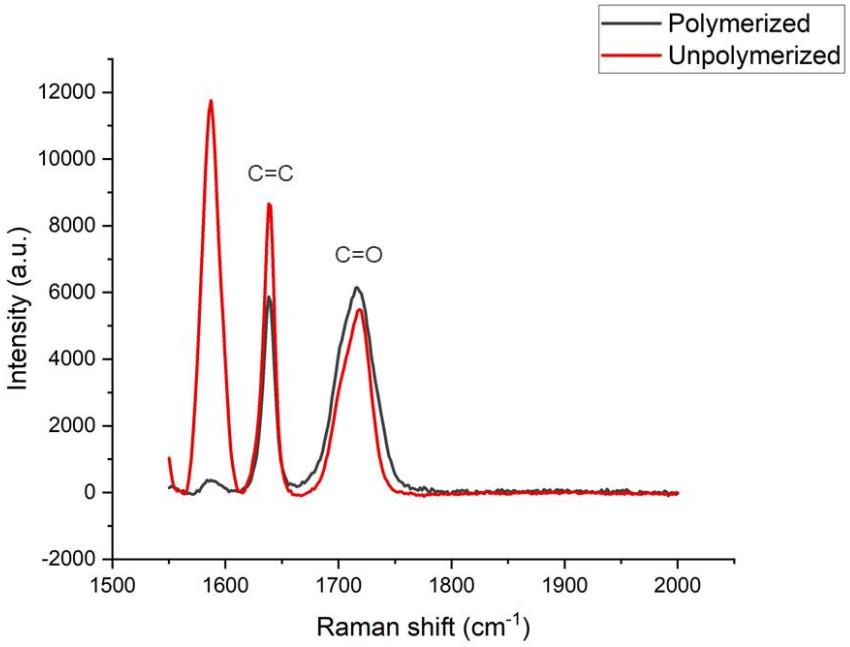

Figure 13. The Raman spectra of polymerized (in black) and unpolymerized (in red) IP-Q samples.

The double carbon bond (C=C) has a distinctive peak around 1635 cm^{-1}, while the double carbon oxygen bond (C=O) has a peak around 1715 cm^{-1}. Both these peaks were visible for the two IP-Q samples. The polymerized sample (black) has a decreased intensity for the (C=C)

peak at 1635 cm^{-1} compared to the unpolymerized sample. The unpolymerized IP-Q sample (red) has a distinctive peak at 1590 cm^{-1}, which is associated with the vibrational mode of an aromatic ring. The polymerized sample only has a small peak at 1590 cm^{-1}.

The mechanical behavior of the ear implant

3.2 Compression of pillars

The stress-strain curves of the of pillars printed with two different layer thicknesses for two different print orientations were determined based on the compression testing using DIC (Fig. 14).

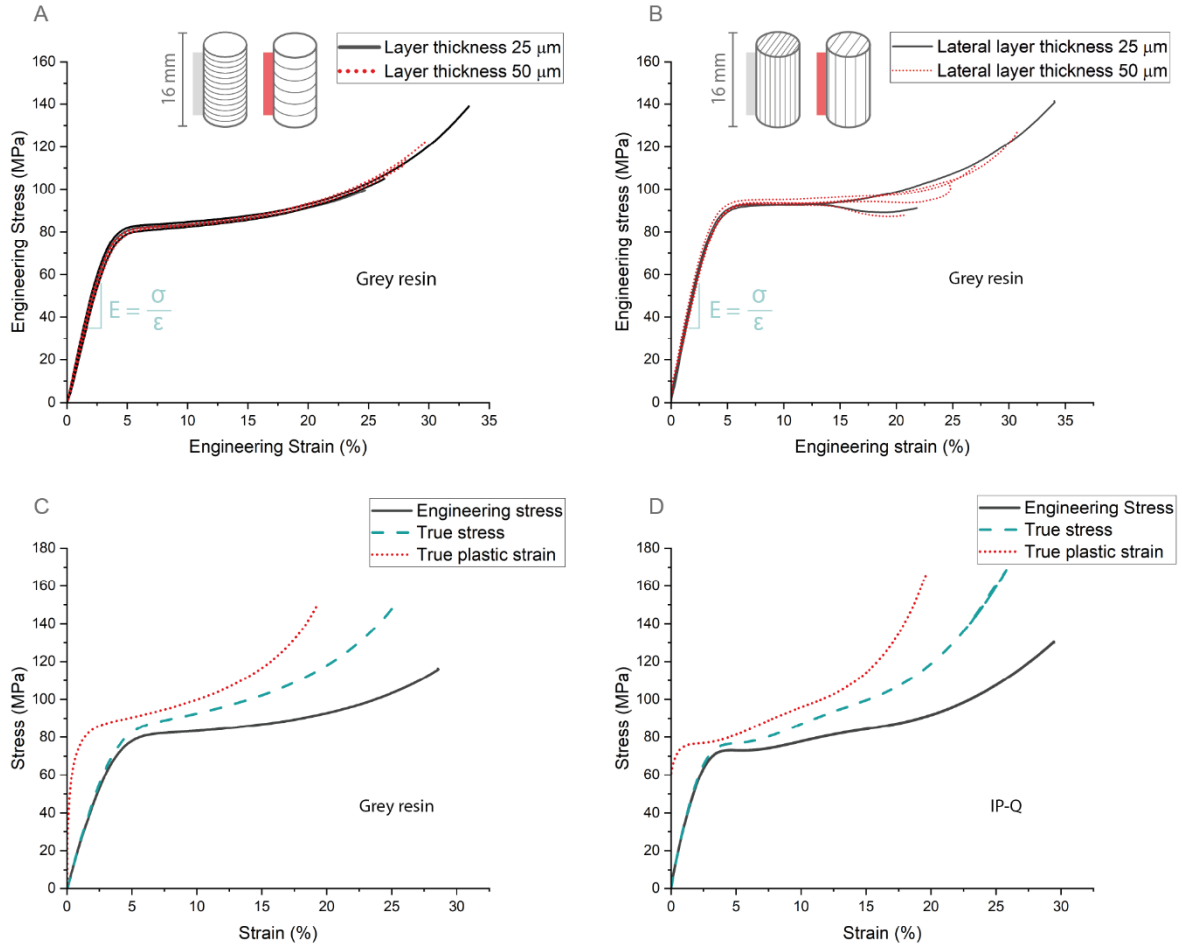

Figure 14. The compression stress-strain curves of (A) grey resin, horizontal printed pillars of 8 Ø mm × 16 mm. (B) SLA grey resin, horizontal printed pillars of 8 Ø mm × 16 mm. (C) The engineering stress-strain, true stress and true plastic strain of grey resin, horizontal printed pillars with layer thickness of 50 µm of 8 Ø mm × 16 m. (C) The engineering stress-strain, true stress, and true plastic strain of IP-Q pillars of 50 µm Ø × 100 µm.

The average Young's modulus for the pillars printed with horizontal layers of 25 µm thickness was 2.51 ± 0.13 GPa and for those with 50 µm thickness, it was 2.50 ± 0.10 GPa. The average yield strength for the 25 µm layer thickness was 59.2 ± 0.91 MPa and for those with 50 µm

thickness it was 56.4 ± 1.7 MPa. The average Young's modulus for the lateral printed pillars with 25 µm layer thickness was 2.51 ± 0.050 GPa and for those with 50 µm layer thickness it was 2.33 ± 0.20 GPa. The average yield strength for the laterally printed pillar with 25 µm layer thickness was 72.4 ± 3.4 MPa and for those with 50 µm layer thickness , it was 79.4 ± 2.8 MPa. For the pillars with layer thickness 25 µm, yield could only be determined for two of the pillars. A summary of these values for the Young's modulus and yield strength can be found in table 4.

Table 4. The average Young's modulus and yield strength for the SLA printed pillars with different printing parameters determined from the stress-strain curves obtained from compression testing.

Pillars	***Layer thickness 25 µm***	***Layer thickness 50 µm***
Horizontal layers	E: 2.51 ± 0.13 GPa	E: 2.50 ± 0.10 GPa
	σ_y: 59.2 ± 0.91 MPa	σ_y: 56.4 ± 1.7 MPa
Lateral layers	E: 2.51 ± 0.050 GPa	E: 2.33 ± 0.20 GPa
	σ_y: 72.4 ± 3.4 MPa	σ_y: 79.4 ± 2.8 MPa

The true stress and true plastic strain were calculated from the engineering stress-strain curve of the grey resin, SLA printed pillars using eq. 2.1-2.3 (Fig. 14C). The same equations were used to calculate the true stress and true plastic strain from the engineering stress-strain curve for the IP-Q pillar (Fig. 14D). The Young's modulus for IP-Q calcualted from the linear part of the curve was 2.78 GPa and the yield strenght was 60.4 MPa.

3.3 Experimental torsion testing on solid SLA torsion specimens

For the three upscaled, solid torsion specimens, the torque versus rotation curves were recorded until failure (Fig. 15A-15C). The largest torsion specimen (EC32) failed at the lowest amount of rotation, while the smallest torsion specimens (EC8) failed at the highest amount of rotation. Failure occurred at 211 ± 9.5° for the EC8 torsion specimens, at 182 ± 22.1° for the EC16 torsion specimens and at 132 ± 20.3° for the EC32 torsion specimens. The failure modes of the specimens were examined, by inspecting the fracture angles of the specimens (Table 5, Fig. 15D-15F) The EC32 torsion specimens all failed close to the base of the cylinder near the cube, while for the EC8 and EC16 specimens the failure occurred both close to the cube and in the cylindrical shaft. The fracture angle of the specimens was largest for the EC8 torsion specimen, which has the smallest cylindrical diameter and was smallest for the EC32 torsion specimen which has the largest cylindrical diameter. SEM images of two EC8 torsion specimens were taken, with a flat and tilted fracture angle. For the tilted fracture angle, hackles seem to be

radiating out from a single origin point, in contrast to the flat angle where there are also hackles visible, but they do not have a single origin point. The tilted angle surface has more elongated markings, more size differences, and relatively larger smooth sections within the roughness of the surface, when compared to the flat angle surface. The flat angle surface has rounder markings with more uniform in size (Fig. 15G-15J).

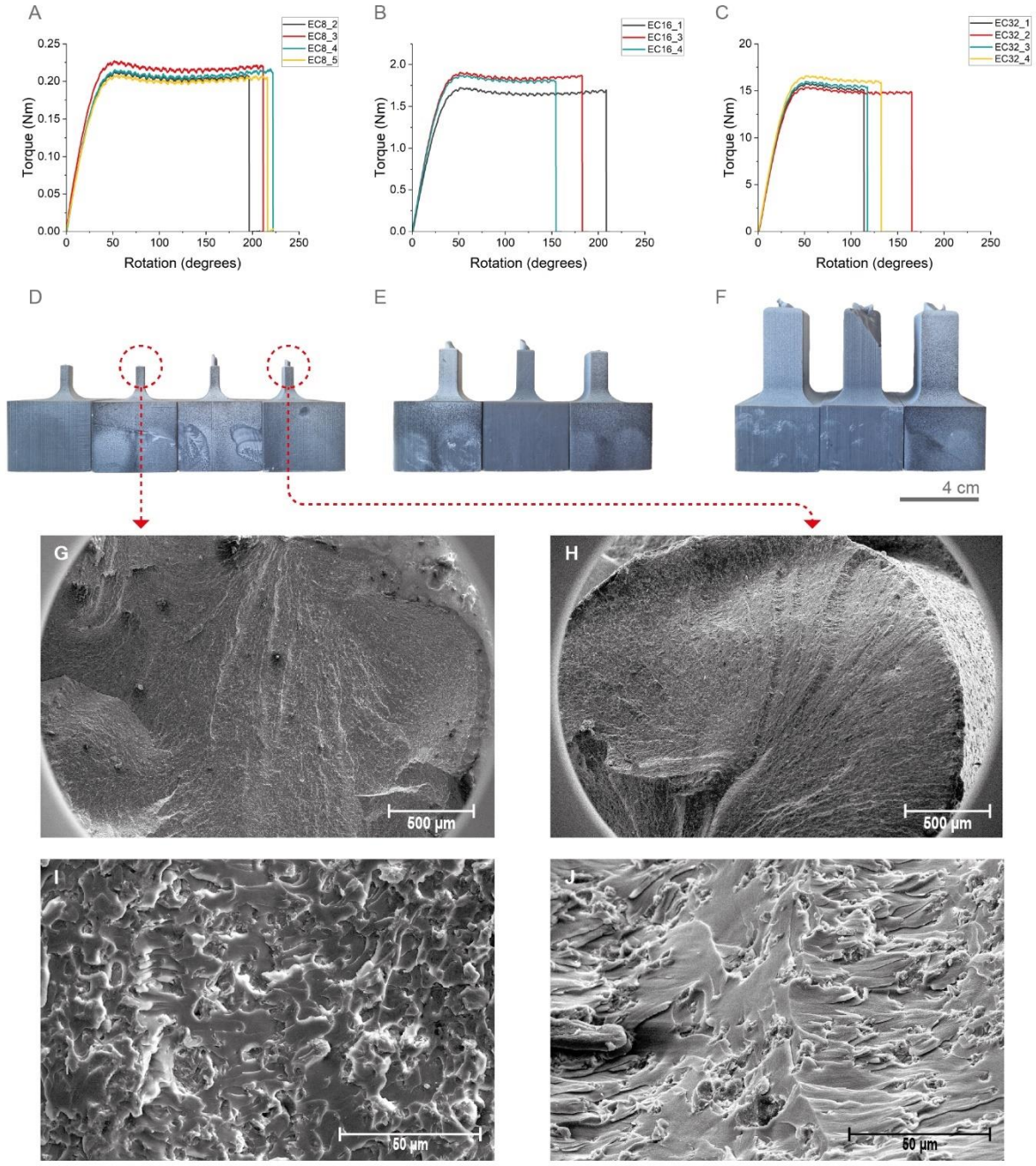

Figure 15. The torque versus rotation curves of the grey-resin, printed torsion specimens EC8 (A), EC16 (B) and EC32 (C). (D, E, F) Images of the fracture angles of the torsion specimens, respectively EC8, EC16 and EC32. (G, I) SEM images of EC8_2 with a flat fracture angle, with magnifications of respectively, 80 × and 1300 ×. (H, J) SEM images of EC8_4 with a tilted fracture angle, with magnification of respectively, 80 × and 1300 ×.

Table 5. Measured angles of the failed torsion specimens printed with grey resin.

Specimen	*EC8*	*EC16*	*EC32*
1	NM	37°	33°
2	NM	36°	NM
3	44°	NM	31°
4	41°	-	-

3.4 Experimental torsion testing versus FEA simulation of the solid SLA EarCube

3.4.1 Torque versus rotation

The behavior of the solid EarCube under torsion was investigated through both FEA modeling and experimental torsion testing of upscaled SLA specimens (which were used to validate the FEA model). The upscaled, solid, torsion specimens were printed in three different sizes (EC8, EC16, and EC32). For each of the torsion specimens, the torque versus rotation was measured. FEA simulations were performed for the three sizes of the torsion specimens as well as on all three sizes for the upscaled EarCubes. The data of the FEA model for the torsion specimens and upscaled EarCubes were plotted against the experimental data obtained from the torsion testing for the linear part of the curve until yield, which is about 50° of rotation (Fig. 16).

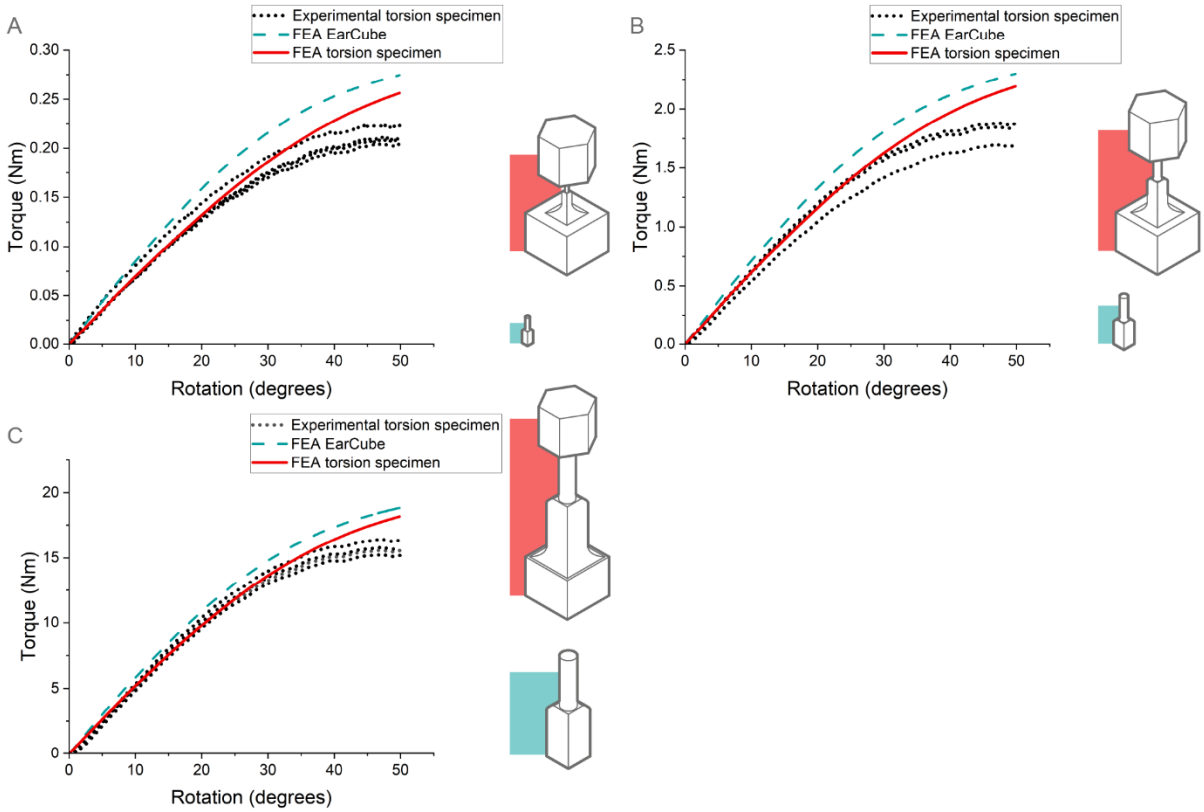

Figure 16. The torque versus rotation graph of the torsion specimens. (A) The experimental data of the EC8 torsion specimens and the FEA data of the EC8 torsion specimen and the EarCube. (B) The experimental data of the EC16 torsion specimens and the FEA data of the EC16 torsion specimen and the EarCube. (C) The experimental data of the EC32 torsion specimens and the FEA data of the EC32 torsion specimen and the EarCube.

For the three different sizes of torsion specimens, the torque increases with specimen size. The torque for the EC16 torsion specimen was about 8.5 times larger than that of the EC8 torsion specimen and 8.7 times smaller than that of the EC32 torsion specimen. For all sizes of the upscaled specimens it was visible that the FEA data for the EarCube (in blue) showed a higher torque than the experimental data of the torsion specimens (in black). At 15° rotation, the experimental data of the EC8 torsion specimen was 85.6 ± 5.0% of the FEA EarCube data. The EC16 and EC32 torsion specimen experimental data were 84.6 ± 5.1% and 89.2 ± 2.8% of the FEA EarCube data respectively. As the degree in rotation increases, the difference between the FEA data and the experimental data gets larger. At 50° rotation, the experimental data of the EC8, EC16 and EC32 torsion specimens were 77.1 ± 2.6%, 78.5 ± 3.5% and 83.6 ± 2.2% of the FEA EarCube data respectively. The FEA data of the torsion specimens (in red) showed a lower torque than the FEA EarCube data and was more similar to the experimental data. At 15° rotation, the difference between the experimental data and FEA torsion specimen data for the EC8, EC16 and EC32 torsion specimens was 103 ± 6.0%, 99.3 ± 5.9% and 102 ± 3.2% respectively. However, after about 30° of rotation, the torque also becomes higher than the torque recorded for the experimental data.

3.4.2 Shear stress versus shear strain

From the FEA model the shear stress and strain were obtained and compared to the experimental stress and strain data for the three different sized, solid, torsion specimens up to a rotation of 50° (0.87 rad) (Fig. 17). The shear stress-strain curves for the EC8 and EC16 torsion specimens had a lower shear stress than the FEA data shear stress-strain curve (in red). From the shear stress-strain curves the shear modulus was calculated from the linear part of the graph. The EC8 torsion specimens had an average shear modulus of 670 ± 34.0 MPa, for the EC16 torsion specimens it was 772 ± 30.6 MPa, and the EC32 torsion specimens had a shear modulus of 867 ± 36.7 MPa. Using eq. 2.8, the theoretical value for the shear modulus is G = 863 MPa.

The strain distribution of the experimental torsion specimens captured using DIC was compared to the strain distribution created with FEA (Fig. 17). For the EC8 and EC16 torsion specimen (Fig. 17B, 17C) the cubic part of the EarCube has a strain close to zero, similar to the FEA strain distribution (Fig.17E), this was not captured for the EC32 torsion specimen. The EC32 torsion specimen had the highest strain at the junction of the cube and cylinder, which is also the case for the FEA strain distribution.

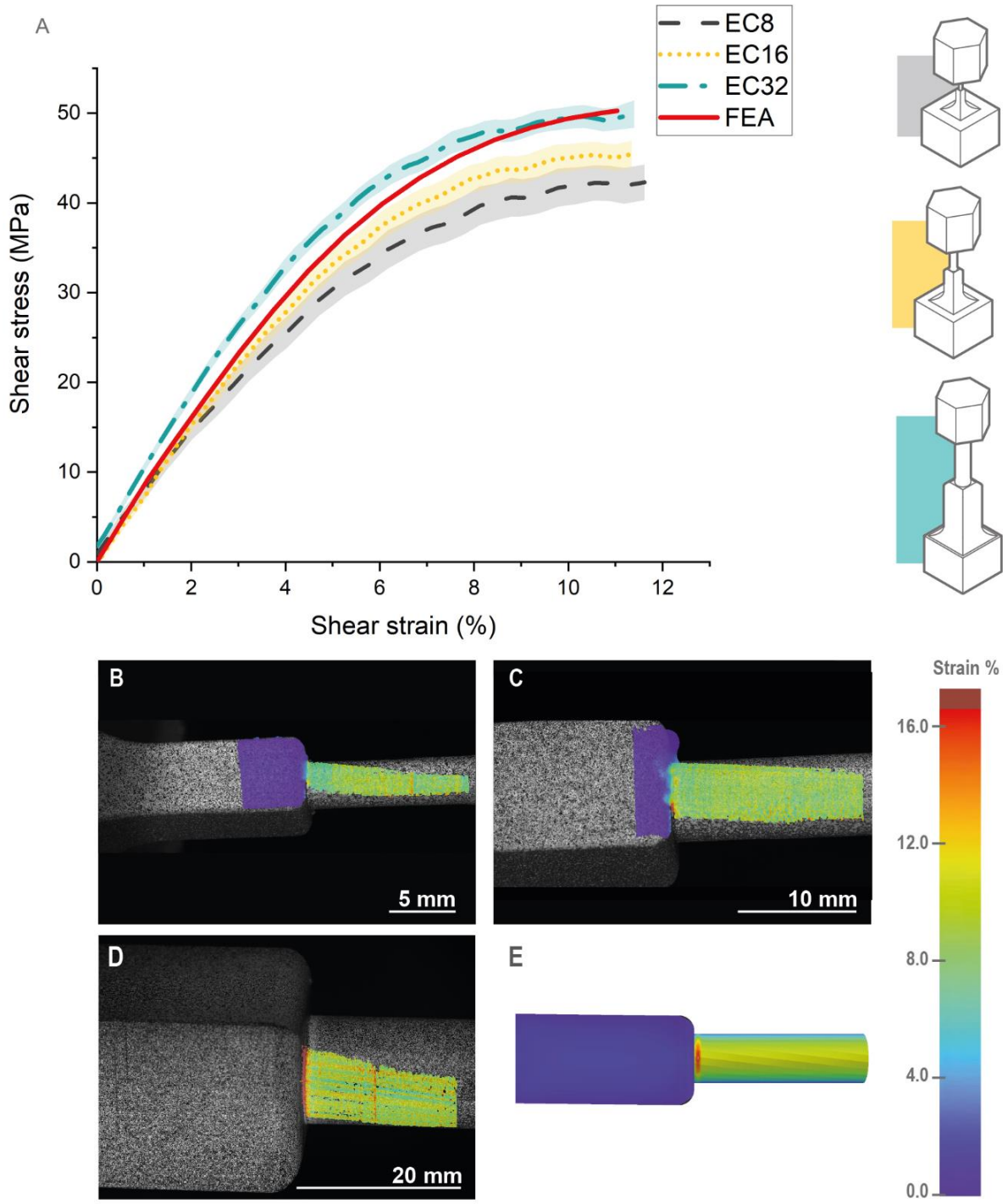

Figure 17. The shear stress-strain curve and distribution computed using DIC. (A) Shear stress versus shear strain from experimental data from the grey-resin-SLA-printed torsions specimens and FEA data (in red). The experimental data was averaged, the shadows of the lines are the mean ± SD. The effective strain (von mises) distribution from DIC for (B) the grey resin EC8 torsion specimen, (C) the grey resin EC16 torsion specimen and (D) the grey resin EC32 torsion specimen. (E) The shear strain distribution from FEA. The color map is in strain percentage in the range of 0% to 16%.

3.5 Experimental torsion testing versus FEA simulation of the porous SLA EarCube

The behavior of the porous EarCube under torsion was also investigated, through both experimental testing and FEA simulation. The porous EarCube was printed in one size (EC32)

with a square unit lattice inner structure. The torque versus the rotation was measured for the porous EC32 specimen and compared to the FEA simulation of the porous upscaled EarCube. The FEA simulation was performed until 40 degrees rotation. The strain distribution of the porous EC32 specimen captured using DIC was also compared to the strain distribution from the FEA simulation (Fig. 18).

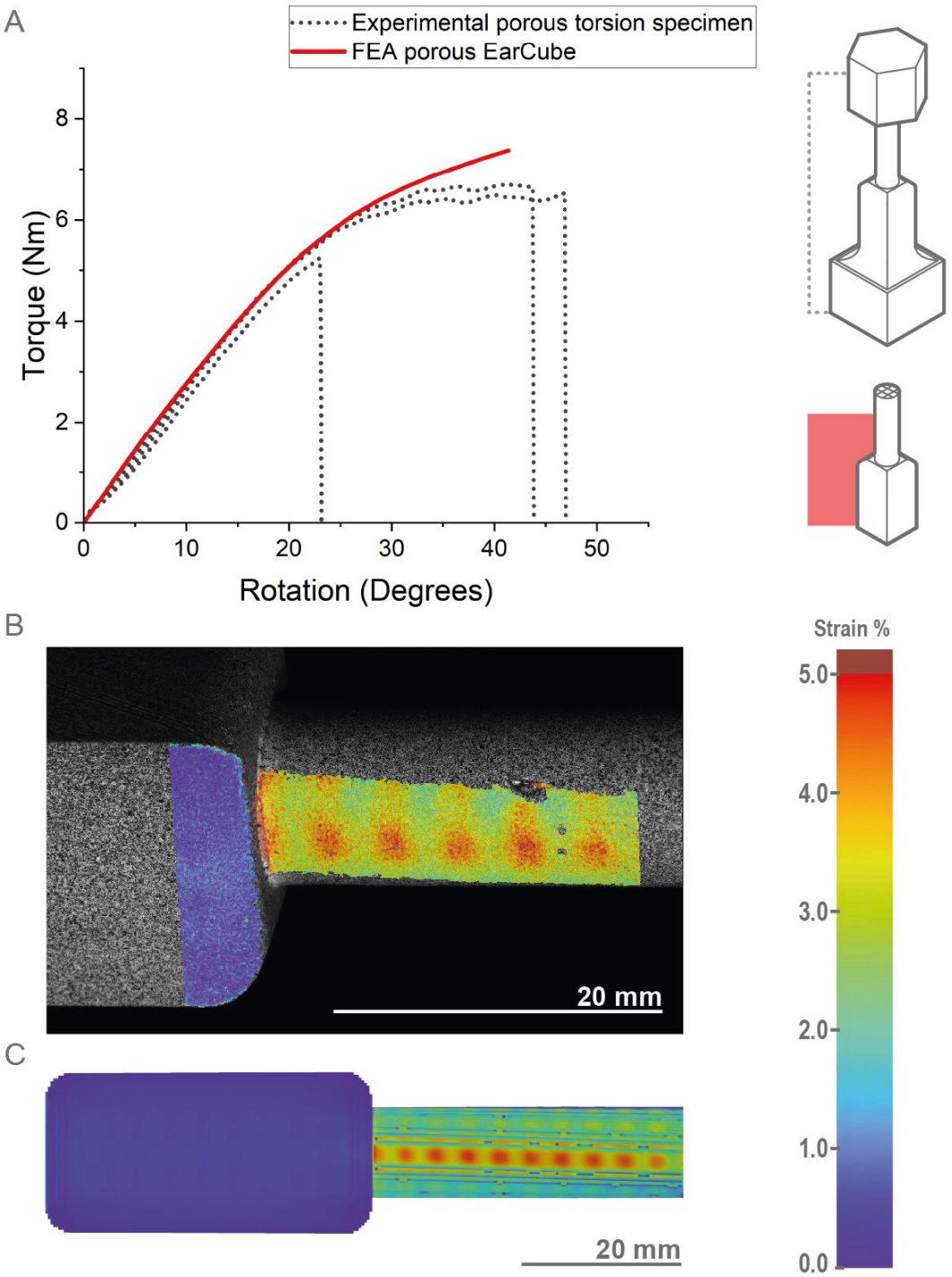

Figure 18. The comparison of the experimental torsion behavior of the porous EC32 specimen and the FEA torsion behavior of the upscaled EarCube. (A) The torque versus rotation graph of the experimental EC32 torsion specimen and the FEA upscaled EarCube. (B) The effective strain (von Mises) distribution from DIC for the porous EC32 torsion specimen at roughly 15° rotation. (C) The shear strain distribution from FEA for the porous upscaled EarCube at roughly 15° rotation.

The three tested specimens had an average rotation at failure of 38 ± 10°. The failure of the porous EC32 torsion specimens occurs at a rotation 3.5 times lower than that of the solid EC32 specimens. The linear part of the experimental curves and the FEA curve show a high similarity, at 15° rotation the experimental data was 98.9 ± 2.8%. After yielding the FEA curve becomes higher than the experimental curves and at 40° (for two of the specimens) the experimental data was 89.1 ± 1.7% of the FEA data. For both the strain distributions (Fig. 18B and Fig. 18C), the cubic part of the EarCube has a strain close to zero. Near the juncture between the cylinder and the cube there is a high strain visible for both the DIC and the FEA image. Both strain distributions show a checkered pattern on the cylinder, which corresponds to the pore size of the inner porous structure.

3.6 Comparison of FEA models with grey resin and IP-Q

The experimental torsion data and FEA torsion data in the previous section was for upscaled grey resin SLA-printed specimens. However, the final ear implant will be printed with IP-Q using 2PP and will be much smaller. The upscaled specimens were chosen to be printed with grey resin using SLA, due to the similarities between the two printing methods and the expected similarities between the two photopolymers. The assumption behind this was that if the FEA data for grey resin was similar to the experimental data, and since IP-Q behaves similarly to grey resin, the FEA data for IP-Q would also likely be similar to the experimental data for IP-Q. The FEA model for the two materials was the same, with the exception of the material properties input. The FEA torsion data for IP-Q cannot be experimentally validated, since the printed specimens were too small for torsion testing. However, the FEA data for both materials can be compared. From the FEA data for the EarCube the shear stress and shear strain were obtained for both grey resin and IP-Q (Fig. 19). The linear part of the stress-strain curve was steeper for IP-Q than for grey resin, and the yield point of the material occurred at a lower shear strain than for grey resin.

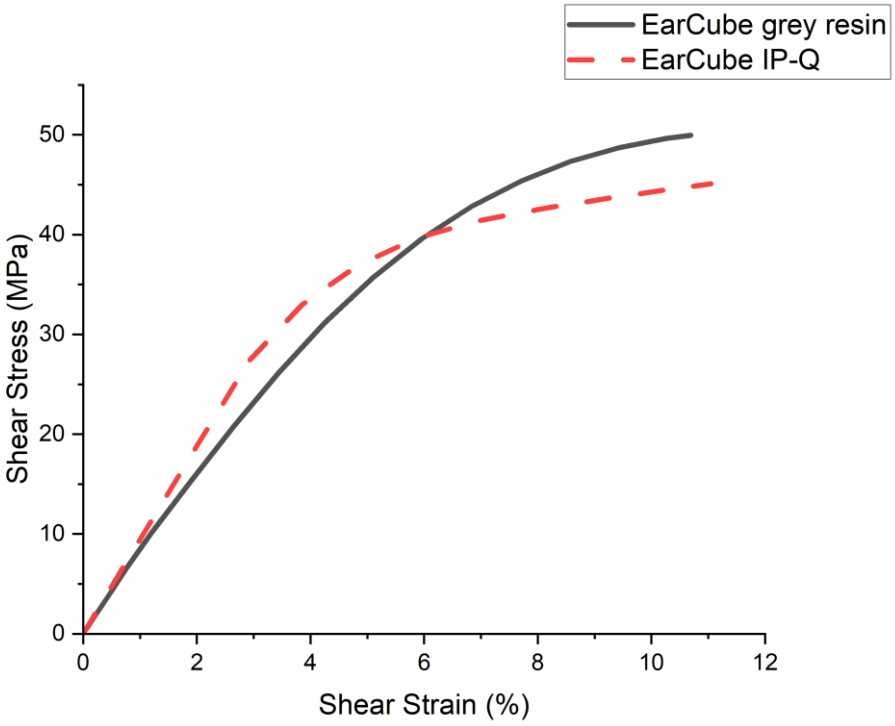

Figure 19. The shear stress versus strain FEA data for the solid EarCube with the material properties of grey resin and the material properties of IP-Q.

3.7 FEA simulation of IP-Q ear implants

Currently there are two potential designs for the ear implants, the EarCube and the BullEar and also two potential designs for the inner porous structure of the ear implant. The final ear implant will not be solid throughout but will contain an internal porous structure for drug storage and release. There are two designs for this porous structure one with pores of 20 μm and another with pores of 60 μm, resulting in a total of four potential designs. The mechanical behavior of these designs under torsion was modeled using FEA for the material IP-Q, focusing on the linear part of the curve until yielding occurred (roughly 50° for the EarCube and 20° for the BullEar).

3.7.1 Comparison of solid and porous EarCube implants

To begin, the behavior of the solid IP-Q EarCube was compared to the behavior of the two porous IP-Q EarCubes with pores of 20 μm and 60 μm. The torque required for both the porous EarCubes was much lower than that of the solid EarCube, with the torque for the EarCube with pores of 20 μm and 60 μm being quite similar to each other. The torque needed to twist the EarCube 15° with pores of 60 μm was 87% of the torque needed for the EarCube with pores of 20 μm. The distribution of the shear stress and shear strain along the solid and porous EarCubes designs, as given by FEA at 15° of rotation were compared (Fig. 20).

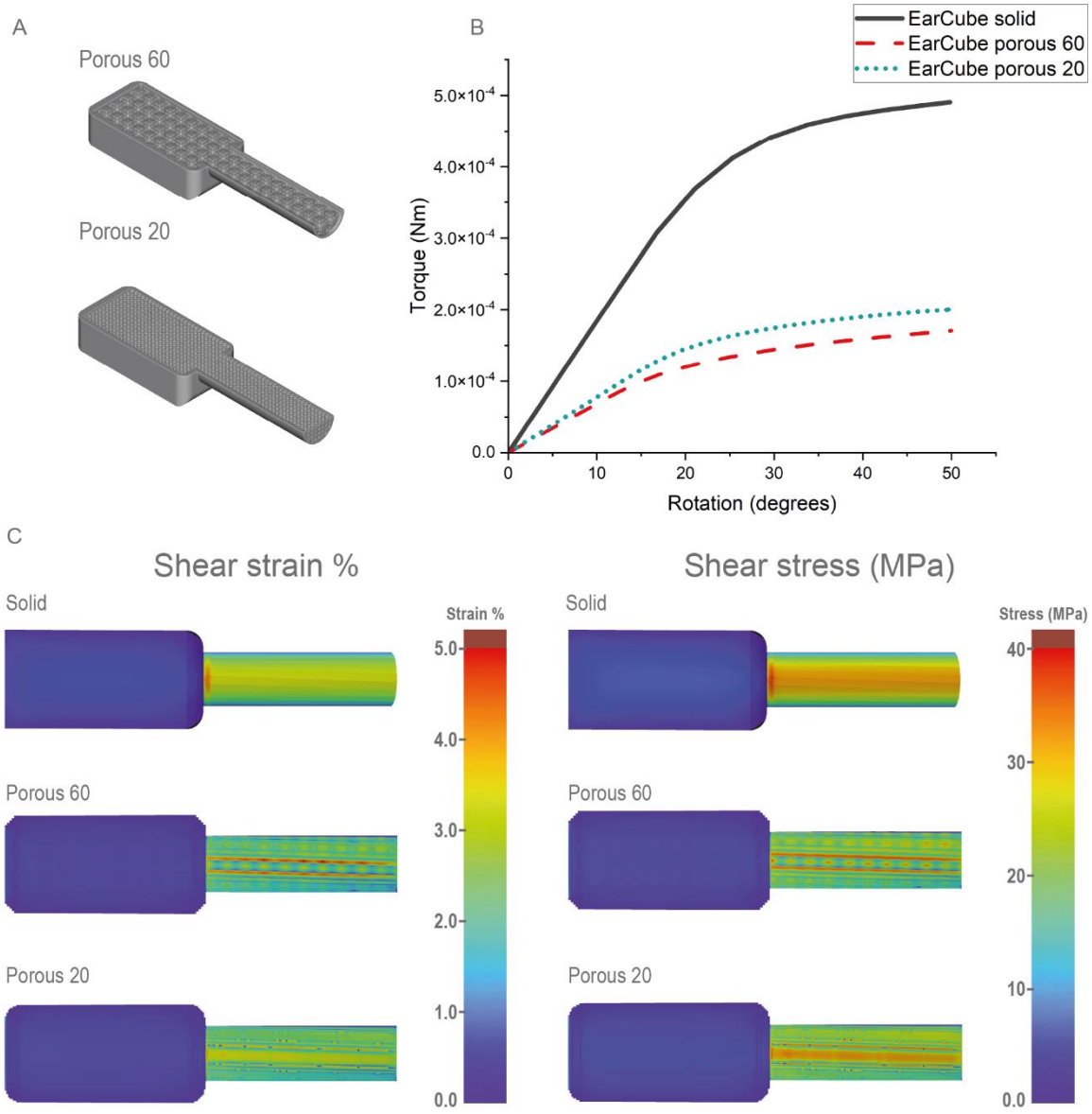

Figure 20. Comparison of the solid and porous EarCube designs. (A) the two porous EarCube designs of 20 and 60 µm. (B) The torque versus rotation graph of the FEA data for IP-Q of the solid EarCube (black), the EarCube with 60 µm pores (red, dashed) and the EarCube with 20 µm pores (blue, dotted). (C) The shear strain (%) and Shear stress (MPa) distribution at 15° rotation from FEA for the solid EarCube (Top), the EarCube with pores of 60 µm (middle) and the EarCube with pores of 20 µm (bottom).

The shear stress and shear strain were limited to the cylindrical part of the EarCube, and in the cube, the shear stress and strain recorded were close to zero. Both the shear stress and shear strain were highest near the junction between the cylindrical part and the cubic part of the design. This peak near the junction was not visible for either of the porous EarCube designs. For the porous 60 design, a checkered pattern was visible in the cylindrical part, corresponding to the pores inside the structure. There were also two lines visible along the length axis of the cylinder, where both the shear strain and shear stress were highest. The porous 20 design

showed no obvious checkered patterns. However, along the length axis of the cylinder a broad line was visible, which has the highest shear stress and strain in the structure (Fig. 20).

3.7.2 Comparison of solid and porous BullEar implants

Torsion testing was also modeled using FEA with the BullEar design for both the solid BullEar and the porous BullEars. The behavior of the solid BullEar under torsion was compared to the behavior of the porous BullEars, with pore sizes of 20 μm and 60 μm (Fig. 21).

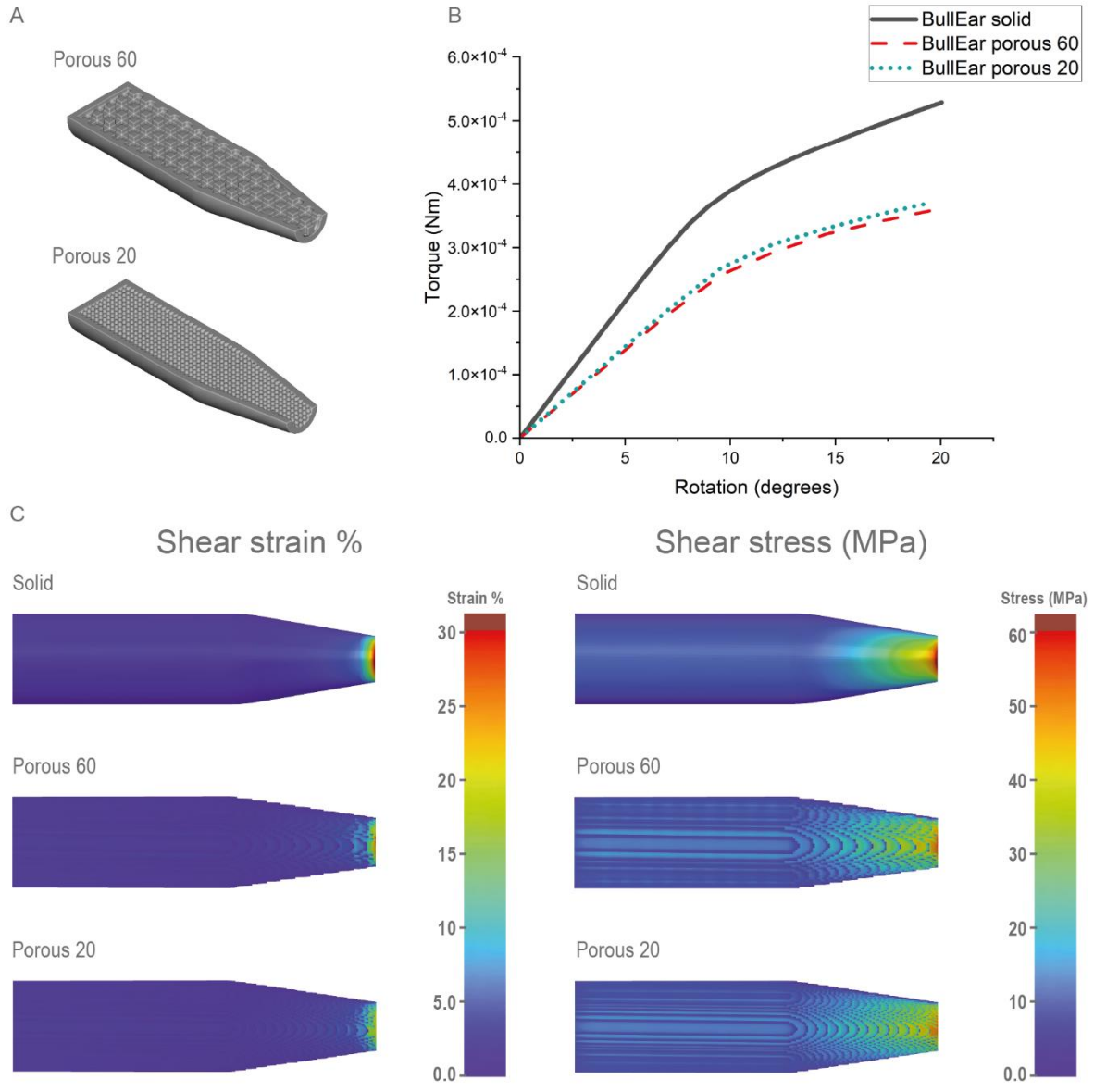

Figure 21. Comparison of the solid and porous BullEar designs. (A) the two porous BullEar designs of 20 and 60 μm. (B) The torque versus rotation curve of the FEA IP-Q BullEar data for the solid BullEar (black), the BullEar with pores of 60 μm (red, dashed) and the BullEar with pores of 20 μm (blue, dotted). (C) The shear strain (%) and Shear stress (MPa) distribution at 15° rotation from FEA for the BullEar (Top), the BullEar with pores of 60 μm (middle) and the BullEar with pores of 20 μm (bottom).

The results showed that the torque required for the solid BullEar was higher than that for torque required for the porous BullEar designs, while the results for both the porous designs were comparable. Specifically, at 15°, the torque needed to rotate the BullEar with pores of 60 μm was 97% of the torque needed to rotate the BullEar with pores of 20 μm. A comparison of the distribution of shear strain and shear stress of the BullEar at 15° rotation as determined by FEA was made (Fig. 21). The distribution of the shear strain was similar for all designs, although the solid BullEar had the highest maximum strain of the three designs, while the design with pores of 20 μm had the lowest maximum strain. The shear strain was concentrated to the tip of the BullEar, where the diameter of the design was the smallest. In contrast, the distribution of the was broader, affecting a larger area of the top of the BullEar. However, the highest levels of shear stress, were still found at the tip of the BullEar for all designs.

3.7.3 Comparison of the EarCube and BullEar design

Finally, the behavior of the two different ear implant designs was compared for both the solid and porous models of both designs (Fig. 22). When comparing the two solid designs, it was observed that more torque was required for the BullEar to produce the same amount of rotation as the EarCube, roughly 1.6 times more. The same was true for the porous EarCube when compared to the porous BullEar, for the 60 μm pores it required 3.1 times more torque to rotate the BullEar and for the 20 μm pores it required 2.7 time more torque at 15° rotation.

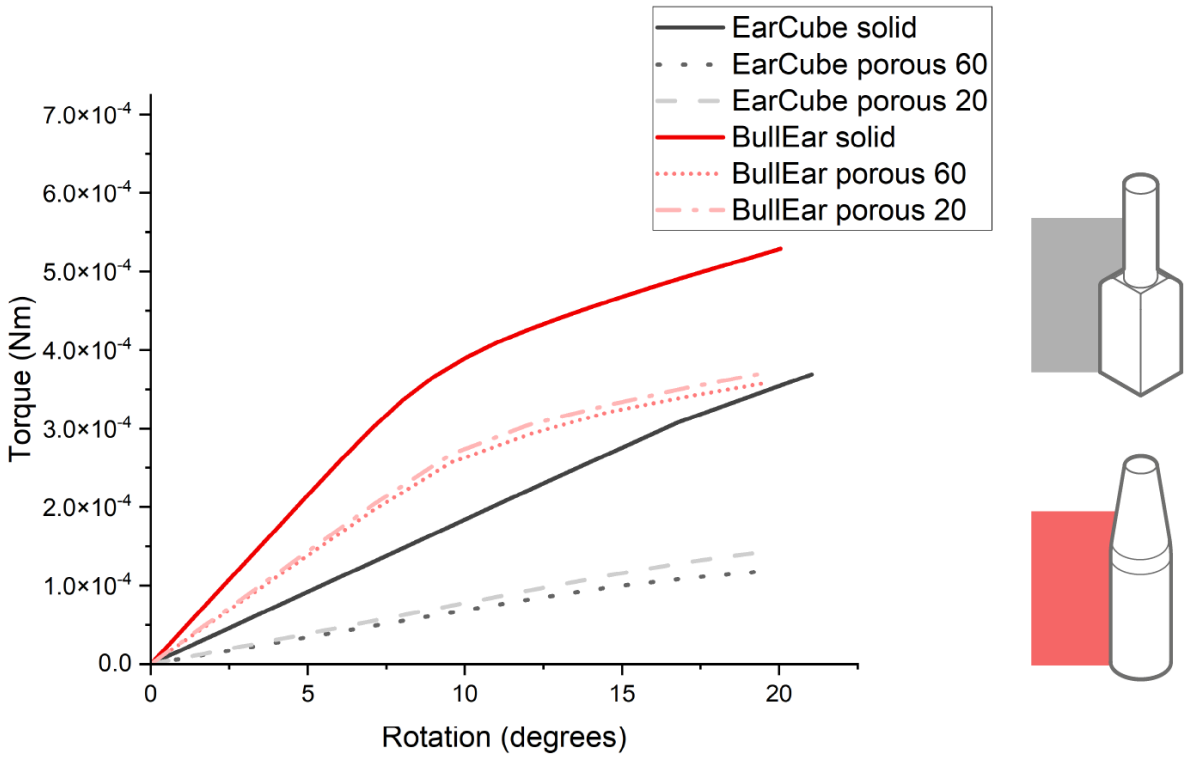

Figure 22. The torque versus rotation graph of the FEA data for IP-Q of the solid and porous EarCube and the solid and porous BullEar design.

4 Discussion and Outlook

In the following chapter, the interpretation of the presented results will be discussed. Mechanical testing of the ear implant designs required a novel approach as, due to the small size of the ear implant, mechanical characterization of the implant using standard mechanical testing equipment was not possible. In this thesis, an alternative method was used characterize the mechanical properties of the ear implant. An FEA torsion model was created, to simulate torsion testing on the ear implant. This model was experimentally validated on upscaled ear implants, printed with SLA, a 3D printing method with the same basic principle as 2PP. Extrapolating this validation to the 2PP ear implants, gave us an approach to characterizing the IP-Q ear implants. The mechanical characterization of the ear implants was necessary because the implant will be subjected to mechanical stressed during its lifetime. Using the FEA simulation data, the mechanical behavior of the two implant designs was compared to determine which design will be most capable of withstanding the mechanical stresses occurring during implantation.

4.1 Raman spectroscopy

The polymerization that occurs during 2PP printing was characterized by performing Raman spectroscopy on untreated IP-Q resin and on IP-Q resin printed with 2PP. During the 2PP process, polymerization occurs which changes the molecular structure of the photoresin by breaking the C=C bond and turning it into single carbon bonds (Fig. 4). This process was made visible by Raman spectroscopy, which shows distinctive peaks for different intramolecular bonds. The C=C bond, found at 1640 $^{cm-1}$, was lower for the polymerized sample of IP-Q than for the unpolymerized sample, which is as expected for a photoresin undergoing polymerization [19-20]. Additionally, for unpolymerized IP-Q, a peak was also visible at 1590 cm^{-1}, which is associated with the aromatic ring. The aromatic ring peak is specific to IP-Q and does not show up (at this intensity) for most other photoresins [13, 19-20, 27-28]. The decrease in intensity of the aromatic ring peak after polymerization, suggests it might also be involved during the polymerization process of IP-Q, a resin specifically designed for high-speed fabrication. As an aromatic ring also contains C=C bonds, this could influence the intensity of the C=C bond peak, which in turn can influence the DC calculations. Therefore, further testing on IP-Q might provide further insight on the specifics of the polymerization process that occurs during the printing of this novel resin.

4.2 Compression testing

Compression testing was performed on pillars printed with grey resin, using different printer settings. Two different layer thicknesses were used (25 and 50 μm) and two different print orientations (horizontal and lateral layers). The Young's modulus was determined for each of these four conditions (Fig. 14, Table 4). In the case of the horizontal printed pillars, the Young's modulus for the pillars printed with a 25 μm layer thickness was 2.51 ± 0.13 GPA and for 50 μm layer thickness it was 2.50 ± 0.10 GPa. The lateral printed pillars had a Young's modulus of 2.51 ± 0.050 GPa for the pillars printed with a 25 μm layer thickness and 2.33 ± 0.20 GPa for the 50 μm layer thickness pillars. When performing a two-sample t-test, to assess if the population means were equal, for all cases the p value was larger than 0.05. This indicates no statistical significant difference between the populations means, although it should be noted that for all these population the sample size was small. The Young's modulus of the material did not change by printing with different layer thicknesses or with different print orientations.

The lack of difference in the Young's modulus between the pillars with different layer thickness was unexpected, as previous research on specimens with different layer thicknesses observed a difference in tensile strength and the Young's modulus [29-30]. Literature is divided on if different print orientations should have an affect on the Young's modulus of the material. Some studies found that SLA printed parts are broadly isotropic materials and print orientation do not affect the Young's modulus [31-34], which is in agreement with our findings. However, others found that there is a dependence of the mechanical properties on the print orientation [30, 35-36]. Most of these tests are performed using tensile testing, making it harder to compare to the compression testing we performed. A larger study into the anisotropy of the SLA materials, possibly using different mechanical tests, is needed to make any definitive statements.

4.3 Torsion failure mode

One of the components of the mechanical behavior of a material, is the failure mode of the material. Two general failure modes are observed in materials, a ductile failure, and a brittle failure [38]. The experimental torsion testing performed on the grey resin torsion specimens were conducted until failure of the specimen. To determine the failure mode of the material, various aspects of the material were taken into account, first the shape of the torque versus rotation curves, second the failure angles of the torsion specimens and lastly scanning electron microscopy (SEM) images of the fracture surface.

From the experimental torque versus rotation curves for all three specimens, it can be observed that after roughly 50° rotation, the materials yields, and as rotation increases, the torque stops increasing (Fig. 15). This is indicative of a ductile material, as they show a large area under the stress-strain curve, since deformation continues after the yield point [38]. However, the failure of the materials occurred at high speed and force, especially the EC32 specimens, which is more indicative of a brittle failure.

Next, the failure angles of the specimens were analyzed. When it comes to ductile materials, failure due to torsion typically occurs along the plane of maximum shear stress, since they are weaker in shear, which is perpendicular to the axis of the structure. In contrast, brittle materials are weaker in tension and therefore torsion failure tends to occur along the plane of maximum tension, which has a 45° angle [39-40]. Of the ten analyzed failure angles, three of them (two EC8 and one EC16 torsion specimen) have a failure angle perpendicular to the axis of the

structure, indicating shear failure. The other six measured specimens have failure angles between 31° and 44°, which indicates that these specimens are weaker in tension than in shear. This indicates that the majority of the torsion specimens had a brittle failure mode.

Finally, SEM images were taken of the fracture surface of two EC8 torsion specimens, one with a flat failure angle and one with a tilted failure angle. Both specimens have a rough surface with micropatterning and fibrillations visible, with the flat angle specimen having an overall smaller micropatterning than the tilted angle specimen. A study that looked at the fracture surfaces of SLA printed tensile specimens showed that for specimens with a very ductile stress-strain curve, the fracture surface was smooth and as the stress-strain curve become more brittle, the fracture became rougher [41]. However, this is not the case for our torsion specimens, as they also show a ductile stress-strain curve, but do not have a smooth fracture surface.

In summation, the difference aspects of the failure mode that were examined mostly indicate that the grey resin material showed a brittle failure. The only exception was the shape of the torque-rotation curve. Additional torsion testing to examine the post-yield plastic behavior of the material, could clarify this inconsistency. Knowing the failure mode of grey resin, can inform the further potential uses of this material.

4.4 Experimental data versus FEA data for torsion testing

The experimental torsion tests on the grey resin torsion specimens were compared with the simulated torsion tests using FEA, for both the solid and porous specimens. When comparing the FEA and experimental torque-rotation curves for the solid specimens, there was good agreement for the elastic-linear part of the curve up to yielding. The porous EC32 specimen also showed good agreement between the experimental and FEA curves, although the porous specimens failed much sooner than the solid specimens and this was not modeled using FEA. Although the linear part of the FEA simulation of torsion testing showed good agreement, the post-yield behavior was different. After yield, the behavior of the solid EarCube is not accurately simulated with FEA using the stress-strain curve of the compression testing as input data. In the stress-strain curve from the compression testing of the grey resin pillars, strain hardening is visible, which is not visible during torsion testing. Therefore, using compression stress-strain curves as input data for FEA is not accurate for simulating post-yield behavior during torsion testing.

Both the solid upscaled EarCube and the solid torsion specimen were simulated using FEA, and the EarCube showed a higher torque for all three sizes. This indicates that the inclusion of the added structures to the EarCube lowers the torque-rotation curve. As the rotation increases, the difference between the FEA data and the experimental data increases. This difference between experimental data and FEA data is smaller for the EC32 torsion specimens than for the EC8 and EC16 torsion specimens. This size dependency might be due to the added structures (the same for the three different sized specimens), which for the EC8 torsion specimens is more relatively added length than for the EC32 torsion specimens.

For the shear stress-strain curves, the shear stress and strain are calculated by approximating the EarCube as only its cylindrical part, since this part has a much smaller diameter than the cubic part and will hold most of the generated stress and strain. Based on the experimental and FEA strain distribution in the EarCube, this assumption seems to hold true, as there is little to no strain observed in the cubic part. Similar to the torque-rotation curves, the elastic-linear region of the stress-strain curves showed good agreement between the experimental and FEA curves. For the shear stress-strain curves, a trend is visible, where the EC8 and EC16 torsion specimens deviate more from the FEA shear stress-strain curve than the EC32 torsion specimens, a trend that is also visible for the torque-rotation curves. The strain distribution for both the solid and porous torsion specimens, showed similar patterns between the experimental DIC distribution and the FEA strain distribution. For the porous EC32 torsion specimen, both showed a checkered pattern with square-like areas having a much higher strain than the surrounding area. These areas are similar in size to the pore size of $1.9 \times 1.9 \times 1.9$ mm^3 and therefore most likely correspond to the inner unit lattice structure. For FEA the higher strain areas on the cylinder occur in between the struts of the inner lattice structure. Since the pattern is so similar, most likely this is also the case for the experimental DIC distribution. Both for the porous and for solid specimens, the experimental data of IP-Q showed good agreement with the FEA model in the linear region. This was the case for the torque-rotation and stress-strain curves, as well as the strain distributions. Therefore, in the linear-elastic region, grey resin can be modeled accurately with FEA using compression data as input.

4.5 FEA model of grey resin versus IP-Q

SLA and 2PP are two additive manufacturing techniques which both utilize the principle of polymerization. However, for SLA only one photon is absorbed, while for 2PP, this is two

[22,42]. The theory is that due to the similar manufacturing process of these two techniques and due to the similar mechanical properties of the two materials used (grey resin and IP-Q), the mechanical behavior of the printed structures will also be in the same range. The Young's modulus for grey resin (printed with SLA) and IP-Q (printed with 2PP) are in the same order of magnitude and are, 2.50 and 2.78 GPa, respectively. The 2PP structures cannot be printed large enough to be able to perform torsion testing and validate the FEA model of the torsion testing on IP-Q. However, with grey resin, large enough specimens can be printed to perform torsion testing and therefore experimental validation of the FEA model is possible. For the linear part of the experimental and FEA data, the data is in agreement. From this validation we extrapolate that when using the same method for FEA we can also simulate the linear part of the IP-Q Ear implant behavior.

The input of IP-Q for FEA was the Young's modulus and the stress-strain curve obtained by compression testing (just as for grey resin). However, this compression data was obtained from a single compression experiment, unlike the grey resin data, which was obtained from three compression experiments on three different pillars. This means that the IP-Q input data, is not as reliable as the input data of grey resin. Nonetheless, the shear stress-strain curves for both materials, obtained from FEA (Fig. 19), do have an overall similar shape, although the materials have a different Young's modulus and yield point. This similarity again suggests that the behavior of IP-Q under torsion can be simulated using FEA using the same techniques as for grey resin. Being able to use FEA modeling to characterize IP-Q, could reduce the need for specialized equipment and make the mechanical testing of more complex designs possible.

4.6 Comparing the mechanical behavior of two ear implant designs

For IP-Q, both the EarCube and the BullEar were simulated using FEA, in both porous and non-porous form. Adding porosity to the designs caused each implant to decrease in stiffness and in mechanical strength. The difference in stiffness and mechanical strength between the two porous structures is not very big, but the decrease varies strongly between the two designs. At 15° rotation, the BullEar design only decreases in stiffness and mechanical strength by 3%, while for the EarCube the difference is 13%. This indicates that the porous structure affects the mechanical properties of the EarCube more so than those of the BullEar. The shear stress-strain distribution of the porous EarCube shows a patterning for both the porous 60 and 20, which is not present on the solid EarCube. This might indicate that there are stress concentrations due to

the square unit lattice inner structure, which can happen near the connection between strut elements where there are sharp transitions [43]. This patterning is not visible on the porous BullEar, and the shear stress-strain distribution of both the solid and porous BullEar are similar. The BullEar is stiffer than the EarCube and has higher mechanical strength. Therefore, the implant to move forward with, from a mechanical properties point of view, is the BullEar.

Characterizing the mechanical properties of these two different designs of the inner ear implants was novel for several reason. It was done using a novel resin (IP-Q) and it was also the first time these type of ear implants have been characterized in this way. The data obtained here will aid in helping to determine if the implants are strong enough to survive the mechanical stress during implantation. This knowledge, among other things, is required to determine if this type of ear implant is a feasible new method of treating inner ear disorders.

4.7 Outlook

In the following section, some recommendations and suggestions for follow-up experiments will be given. First of all, as discussed, the FEA data showed good agreement with the experimental data, although only the linear part until yielding could be accurately modeled using the materials compression data as input for the plasticity. The compression data shows strain hardening, which is not present for the experimental torsion testing of the grey resin torsion specimens. Based on that we assume it would also be absent for torsion testing of the IP-Q specimens. To be able to accurately model the post-yield behavior of the ear implants, another way to model the plasticity needs to be found.

Furthermore, the current inner porous designs of the ear implant are an interconnected network of square unit lattices, with pores and lattices of equal width and height, which are 20 and 60 µm for the two different designs. The inner structure contains sharp transitions which can lead to stress concentrations. To bypass the possible negative effects of these, the inner structure could also be designed so that there are no discontinuities or self-intersecting elements. An example of these are triply periodic minimal surfaces (TPMS), which are also found in nature. Some of these TPMS structures can have superior mechanical properties in comparison to strut-based or other types of structures [38,42]. A next step in the research could be to print ear implants with a TPMS inner structures and compare the mechanical properties with the square unit lattice inner structure ear implants.

Finally, the mechanical properties of the ear implant are not the only aspects to take into consideration. The drug storage, and diffusion of the ear implant and fixation in the cochlear are also important factors in deciding which ear implant design is more suitable. All these factors are also capable of influencing the mechanical properties of the implant. Therefore, in order to make a final decision about the ear implant design, research comparing the results of these additional factors and the proposed changes above is a necessity.

Conclusions

Studying the mechanical behavior of millimeter-sized ear implants is challenging and has not been done before. Using FEA models and scaled-up printed ear implants for validation, the linear part of the mechanical behavior of millimeter-sized ear implants was successfully characterized. The ear implants were printed using 2PP with a novel resin IP-Q and the upscaled ear implants were printed using SLA with grey resin. Using compression data of the grey resin material, the torsion testing of the upscaled EarCubes was accurately simulated until yield using FEA. This validation was extrapolated to indicate that we could also model torsion testing until yield for IP-Q, using compression data of IP-Q. We modeled both ear implant designs with IP-Q using FEA, for both sizes of the porous structure (20 and 60 μm). This showed that the BullEar has a higher stiffness and mechanical strength than the EarCube. The two implants were also tested with two differently sized porous structures. The difference in mechanical performance between the two pore sizes was small and therefore other factors, such as the storage and diffusion of drugs, will determine which porous structure will be used in the final design. From a mechanical point of view, the design to move forward with is the BullEar.

References

[1] K. Nguyen, J. S. Kempfle, D. H. Jung, and C. E. McKenna, “Recent advances in therapeutics and drug delivery for the treatment of inner ear diseases: a patent review (2011-2015),” *Expert Opin. Ther. Pat.*, vol. 27, no. 2, pp. 191–202, 2017, doi: 10.1080/13543776.2017.1252751.

[2] H. Sajjadi and M. M. Paparella, “Meniere’s disease,” *Lancet*, vol. 372, no. 9636, pp. 406–414, 2008, doi: https://doi.org/10.1016/S0140-6736(08)61161-7.

[3] Z. Zhang, X. Li, W. Zhang, and D. S. Kohane, “Drug Delivery across Barriers to the Middle and Inner Ear,” *Adv. Funct. Mater.*, vol. 31, no. 44, pp. 1–12, 2021, doi: 10.1002/adfm.202008701.

[4] B. Szeto, H. Chiang, C. Valentini, M. Yu, J. W. Kysar, and A. K. Lalwani, “Inner ear delivery: Challenges and opportunities,” *Laryngoscope Investig. Otolaryngol.*, vol. 5, no. 1, pp. 122–131, 2020, doi: 10.1002/lio2.336.

[5] J. Hao and S. K. Li, “Inner ear drug delivery: Recent advances, challenges, and perspective,” *Eur. J. Pharm. Sci.*, vol. 126, pp. 82–92, 2019, doi: https://doi.org/10.1016/j.ejps.2018.05.020.

[6] M. Gehrke *et al.*, “Hybrid Ear Cubes for local controlled dexamethasone delivery to the inner ear,” *Eur. J. Pharm. Sci.*, vol. 126, no. December 2017, pp. 23–32, 2019, doi: 10.1016/j.ejps.2018.04.045.

[7] M. Gehrke *et al.*, “Ear Cubes for local controlled drug delivery to the inner ear,” *Int. J. Pharm.*, vol. 509, no. 1, pp. 85–94, 2016, doi: https://doi.org/10.1016/j.ijpharm.2016.04.003.

[8] M. Nouri-Goushki *et al.*, “3D Printing of Large Areas of Highly Ordered Submicron Patterns for Modulating Cell Behavior,” *ACS Applied Materials and Interfaces*, vol. 12, no. 1. pp. 200–208, 2020, doi: 10.1021/acsami.9b17425.

[9] J. Song, C. Michas, C. S. Chen, A. E. White, and M. W. Grinstaff, “From Simple to Architecturally Complex Hydrogel Scaffolds for Cell and Tissue Engineering Applications: Opportunities Presented by Two-Photon Polymerization,” *Adv. Healthc. Mater.*, vol. 9, no. 1, p. 1901217, 2020, doi: https://doi.org/10.1002/adhm.201901217.

[10] A. J. G. Otuka, N. B. Tomazio, K. T. Paula, and C. R. Mendonça, “Two-photon polymerization: Functionalized microstructures, micro-resonators, and bio-scaffolds,” *Polymers (Basel).*, vol. 13, no. 12, pp. 1–30, 2021, doi: 10.3390/polym13121994.

[11] Nanoscribe, “IP Photoresins.” https://www.nanoscribe.com/en/products/ip-photoresins (accessed Nov. 30, 2022).

[12] S. Schweiger, T. Schulze, S. Schlipf, P. Reinig, and H. Schenk, “Characterization of two-photon-polymerization lithography structures via Raman spectroscopy and nanoindentation,” *J. Opt. Microsystems*, vol. 2, no. 03, pp. 035001–7, Aug. 2022, doi: 10.1117/1.JOM.2.3.033501.

[13] J. Bauer, A. Guell Izard, Y. Zhang, T. Baldacchini, and L. Valdevit, “Programmable Mechanical Properties of Two-Photon Polymerized Materials: From Nanowires to Bulk,” *Adv. Mater. Technol.*, vol. 4, no. 9, p. 1900146, 2019, doi: https://doi.org/10.1002/admt.201900146.

[14] J. Bauer, A. G. Izard, Y. Zhang, T. Baldacchini, and L. Valdevit, “Thermal post-curing as an efficient strategy to eliminate process parameter sensitivity in the mechanical properties of two-photon polymerized materials,” *Opt. Express*, vol. 28, no. 14, pp. 20362–20371, Jul. 2020, doi: 10.1364/OE.395986.

[15] M. Diamantopoulou, N. Karathanasopoulos, and D. Mohr, “Stress-strain response of polymers made through two-photon lithography: Micro-scale experiments and neural network modeling,” *Addit. Manuf.*, vol. 47, p. 102266, 2021, doi: https://doi.org/10.1016/j.addma.2021.102266.

[16] Q. Hu *et al.*, “The influence of printing parameters on multi-material two-photon polymerisation based micro additive manufacturing,” *Addit. Manuf.*, vol. 51, p. 102575, 2022, doi: 10.1016/j.addma.2021.102575.

[17] E. D. Lemma *et al.*, “Mechanical Properties Tunability of Three-Dimensional Polymeric Structures in Two-Photon Lithography,” *IEEE Trans. Nanotechnol.*, vol. 16, no. 1, pp. 23–31, 2017, doi: 10.1109/TNANO.2016.2625820.

[18] I. Gaytán, M. Burelo, and H. Loza-Tavera, “Current status on the biodegradability of acrylic polymers: microorganisms, enzymes and metabolic pathways involved,” *Appl. Microbiol. Biotechnol.*, vol. 105, no. 3, pp. 991–1006, 2021, doi: 10.1007/s00253-020-11073-1.
[19] L. J. Jiang *et al.*, “Two-photon polymerization: investigation of chemical and mechanical properties of resins using Raman microspectroscopy,” *Opt. Lett.*, vol. 39, no. 10, pp. 3034–3037, 2014, doi: 10.1364/OL.39.003034.
[20] C. Pianelli, J. Devaux, S. Bebelman, and G. Leloup, “The micro-Raman spectroscopy, a useful tool to determine the degree of conversion of light-activated composite resins,” *J. Biomed. Mater. Res.*, vol. 48, no. 5, pp. 675–681, 1999, doi: 10.1002/(SICI)1097-4636(1999)48:5<675::AID-JBM11>3.0.CO;2-P.
[21] Z.-Y. Hu *et al.*, “Two-Photon Polymerization Nanomanufacturing Based on the Definition–Reinforcement–Solidification (DRS) Strategy,” *J. Light. Technol.*, vol. 39, no. 7, pp. 2091–2098, 2021, doi: 10.1109/JLT.2020.3045452.
[22] M. Pagac *et al.*, “A Review of Vat Photopolymerization Technology : Materials,” *Polymers (Basel).*, vol. 13, no. 13, p. 598, 2021.
[23] ASTM standard D20, “Standard Test Method for Compressive Properties of Rigid Plastics. D695-15,” pp. 1–8, 2015, doi: 10.1520/D0695-15.2.
[24] Dassault Systèmes, “ABAQUS 6.14 Getting Started with Abaqus: Interactive Edition,” *ABAQUS 6.14 Get. Started*, p. 693, 2014, [Online]. Available: http://abaqusdoc.ucalgary.ca/books/gsk/default.htm.
[25] J. R. C. Dizon, A. D. Valino, L. R. Souza, A. H. Espera, Q. Chen, and R. C. Advincula, “3D printed injection molds using various 3D printing technologies,” *Mater. Sci. Forum*, vol. 1005 MSF, pp. 150–156, 2020, doi: 10.4028/www.scientific.net/MSF.1005.150.
[26] ASTM standard E28, “Standard test method for shear modulus at room temperature. E143-20,” *Astm*, vol. 87, no. November 2001, pp. 1–6, 1987, doi: 10.1520/E0143-20.2.
[27] M. C. Saldívar, E. L. Doubrovski, M. J. Mirzaali, and A. A. Zadpoor, “Nonlinear coarse-graining models for 3D printed multi-material biomimetic composites,” *Addit. Manuf.*, vol. 58, no. July, p. 103062, 2022, doi: 10.1016/j.addma.2022.103062.
[28] Y. Liu, J. H. Campbell, O. Stein, L. Jiang, J. Hund, and Y. Lu, “Deformation behavior of foam laser targets fabricated by two-photon polymerization,” *Nanomaterials*, vol. 8, no. 7, pp. 1–20, 2018, doi: 10.3390/nano8070498.
[29] J. S. Oakdale, J. Ye, W. L. Smith, and J. Biener, “Post-print UV curing method for improving the mechanical properties of prototypes derived from two-photon lithography,” *Opt. Express*, vol. 24, no. 24, p. 27077, 2016, doi: 10.1364/oe.24.027077.
[30] K. Chockalingam, N. Jawahar, U. Chandrasekar, and K. N. Ramanathan, “Establishment of process model for part strength in stereolithography,” *J. Mater. Process. Technol.*, vol. 208, no. 1–3, pp. 348–365, 2008, doi: 10.1016/j.jmatprotec.2007.12.144.
[31] S. Wang, Y. Ma, Z. Deng, K. Zhang, and S. Dai, “Implementation of an elastoplastic constitutive model for 3D-printed materials fabricated by stereolithography,” *Addit. Manuf.*, vol. 33, no. January, p. 101104, 2020, doi: 10.1016/j.addma.2020.101104.
[32] F. Cosmi and A. Dal Maso, “A mechanical characterization of SLA 3D-printed specimens for low-budget applications,” *Mater. Today Proc.*, vol. 32, pp. 194–201, 2019, doi: 10.1016/j.matpr.2020.04.602.
[33] J. R. C. Dizon, A. H. Espera, Q. Chen, and R. C. Advincula, “Mechanical characterization of 3D-printed polymers,” *Addit. Manuf.*, vol. 20, pp. 44–67, 2018, doi: 10.1016/j.addma.2017.12.002.
[34] R. Hague, S. Mansour, N. Saleh, and R. Harris, “Materials analysis of stereolithography resins for use in Rapid Manufacturing,” *J. Mater. Sci.*, vol. 39, no. 7, pp. 2457–2464, 2004, doi: 10.1023/B:JMSC.0000020010.73768.4a.
[35] S. A. Shanmugasundaram, J. Razmi, M. J. Mian, and L. Ladani, “Mechanical anisotropy and surface roughness in additively manufactured parts fabricated by stereolithography (SLA) using statistical analysis,” *Materials (Basel).*, vol. 13, no. 11, 2020, doi: 10.3390/ma13112496.
[36] J. M. Dulieu-Barton and M. C. Fulton, “Mechanical properties of a typical stereolithography resin,” *Strain*, vol. 36, no. 2, pp. 81–87, 2000, doi: 10.1111/j.1475-1305.2000.tb01177.x.
[37] J. S. Saini, L. Dowling, J. Kennedy, and D. Trimble, “Investigations of the mechanical

properties on different print orientations in SLA 3D printed resin," *Proc. Inst. Mech. Eng. Part C J. Mech. Eng. Sci.*, vol. 234, no. 11, pp. 2279–2293, 2020, doi: 10.1177/0954406220904106.
[38] M. D. Hayes, D. B. Edwards, and A. R. Shah, *Fractography Basics*. 2015.
[39] Y. M. Hailu, A. Nazir, S. C. Lin, and J. Y. Jeng, "The effect of functional gradient material distribution and patterning on torsional properties of lattice structures manufactured using multijet fusion technology," *Materials (Basel).*, vol. 14, no. 21, pp. 1–21, 2021, doi: 10.3390/ma14216521.
[40] H. Sadaghian, S. Khalilzadehtabrizi, M. Farzam, and S. Dehghan, "Behavior of 3D-printed polymers under monotonic torsion – A database of 15 different materials," *Addit. Manuf.*, vol. 60, no. PA, p. 103251, 2022, doi: 10.1016/j.addma.2022.103251.
[41] L. Quagliato, S. Yeon Kim, and S. C. Ryu, "Quasi-ductile to brittle transitional behavior and material properties gradient for additively manufactured SLA acrylate," *Mater. Lett.*, vol. 329, p. 133121, 2022, doi: https://doi.org/10.1016/j.matlet.2022.133121.
[42] S. Waheed *et al.*, "3D printed microfluidic devices: Enablers and barriers," *Lab Chip*, vol. 16, no. 11, pp. 1993–2013, 2016, doi: 10.1039/c6lc00284f.
[43] O. Al-Ketan, R. Rezgui, R. Rowshan, H. Du, N. X. Fang, and R. K. Abu Al-Rub, "Microarchitected Stretching-Dominated Mechanical Metamaterials with Minimal Surface Topologies," *Advanced Engineering Materials*, vol. 20, no. 9. 2018, doi: 10.1002/adem.201800029.

List of Tables

List of Figures

Appendices

A. Convergence study of the FEA torsion model

The convergence study was performed on three different types of elements, C3D8, C3D10 and C3D20R. The convergence study was performed for both the Torque and the shear stress (Fig. 23).

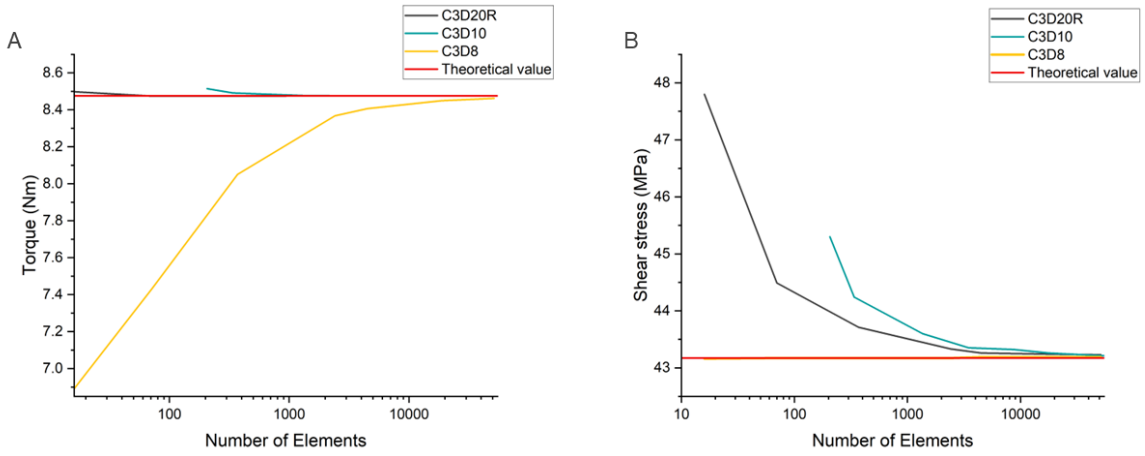

Figure 23. The convergence of the torque and shear stress from the FEA cylinder model to the calculated theoretical value (red). A) The shear stress versus the number of elements in the mesh for the tetrahedral elements (C3D10) and for the hexahedral elements (C3D8 and C3D20R). B) The torque versus the number of elements in the mesh for the tetrahedral elements (C3D10) and for the hexahedral elements (C3D8 and C3D20R).

The theoretical values for the torque and the shear stress were calculated using eq. 2.5-2.8 with a Young's modulus of 2504 MPa, which gives T = 8.48 Nm and τ = 43.17 MPa. The torque for the linear hexagonal element (C3D8) is very slow to converge to the theoretical value, even though the shear stress for C3D8 is the same as the theoretical value from the start. The torque converges to the theoretical value earlier than the shear stress, for the quadratic elements (C3D10 and C3D20R). This convergence of the torque occurs earlier with the C3D20R mesh than with the C3D10 elements, while for the shear stress the convergence is around the same number of elements for both mesh types (Fig. 23).

A final comparison was made between C3D10 and C3D20R, to compare the time it took to compute the model versus the number of elements in the mesh (Fig. 24). The time for the C3D20R mesh increases much faster than for the C3D10 mesh and therefore the C3D10 mesh was used for the solid EarCube and torsion specimen models.

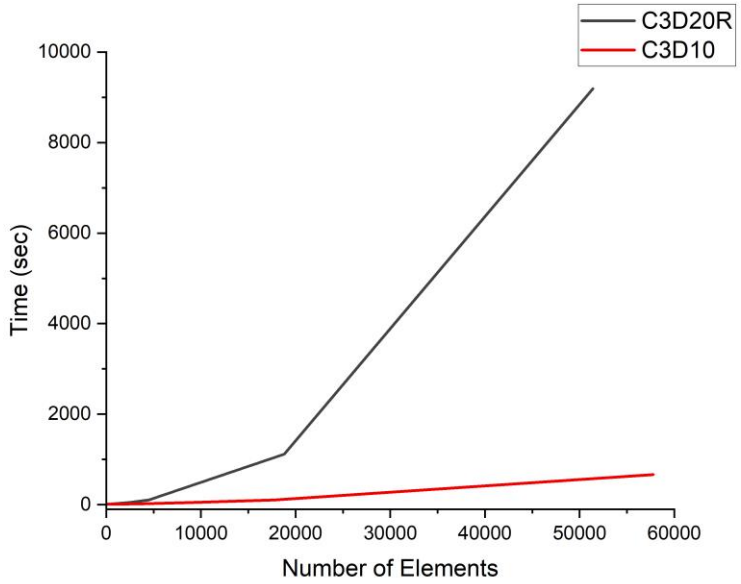

Figure 24. The amount of time (in seconds) it took to compute the model using the C3D10 elements mesh (red) or the C3D20R elements mesh (black).

For all the solid models the C3D10 elements were used for meshing (Fig. 25), and the mesh was refined until the difference for the shear stress for a higher number of elements was less than 1.0%. For example, for the EC16 upscaled EarCube the shear stress did not change more than 1.0% after roughly 25.000 elements and this was therefore the number of elements used in the model (Fig. 26). The convergence of the shear stress was used since the torque converges to a solution for a much coarser mesh.

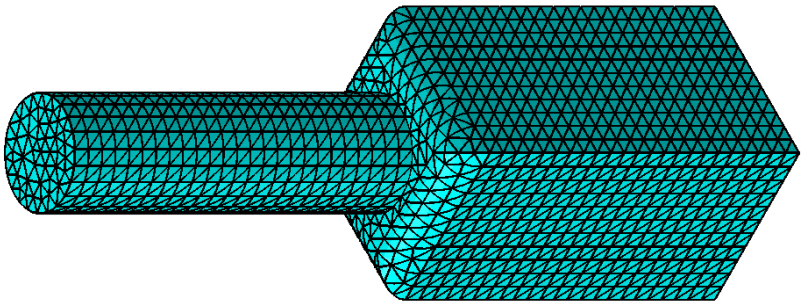

Figure 25. The quadratic tetrahedral mesh (C3D10 elements) on the solid EarCube model.

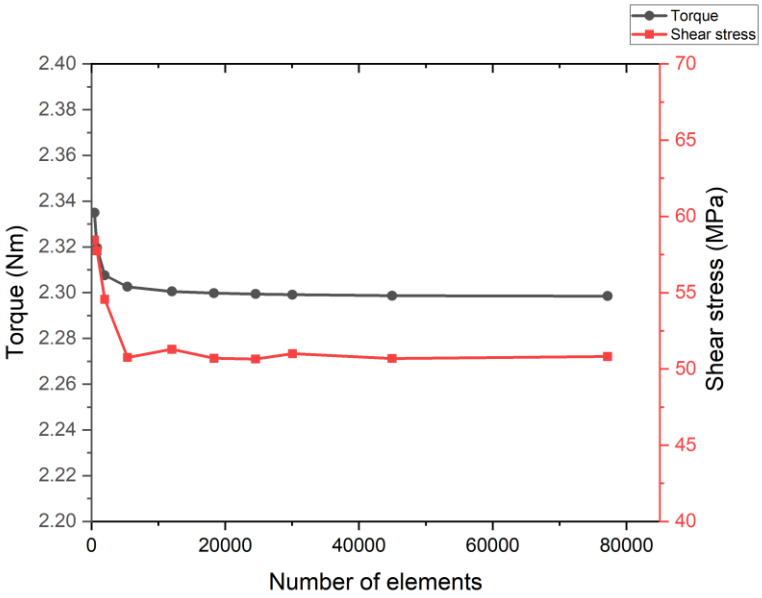

Figure 26. The torque and the Shear stress versus the number of elements used for the mesh for the EC16 EarCube FEA model.